OPTIMIZATION OF SHALE RESOURCE DEVELOPMENT USING REDUCED-PHYSICS SURROGATE MODELS

A THESIS SUBMITTED TO THE DEPARTMENT OF ENERGY RESOURCES ENGINEERING
AND THE COMMITTEE ON GRADUATE STUDIES
OF STANFORD UNIVERSITY
IN PARTIAL FULFILLMENT OF THE REQUIREMENTS FOR
THE DEGREE OF MASTER OF SCIENCE

Kurt Caylor Wilson
May 2012

Abstract

The economics of oil and gas field development can be improved significantly by using computational optimization to guide operations. In this work, we present a general workflow for applying optimization to the development of shale gas reservoirs. Starting with a detailed full-physics simulation model, which includes heterogeneous geology, highly-resolved fracture networks, dual-porosity, dual-permeability regions, and gas desorption, the approach first entails the generation of a much simpler, and much more computationally efficient, reduced-physics surrogate model. The reduced-physics model is tuned using a procedure akin to history matching to provide results in close agreement with the full-physics model. The surrogate model is then used for field development optimization. During the course of the optimization, the surrogate model is periodically retrained to match the full-physics representation of the current best solution.

In the optimizations considered here, we apply a direct search technique (generalized pattern search) and seek to determine the optimal locations, lengths, and number of fracture stages for a set of horizontal wells. In two examples, involving three-dimensional models with heterogenous properties representative of the Barnett Shale, optimization is shown to provide field development scenarios with net present values that are more than double those of base case designs.

Acknowledgements

I would like to acknowledge the many people and institutions who supported my time at Stanford. I wish to thank Dr. Louis Durlofsky for his guidance and support. Lou has a sharp mind and kept my research focused and productive. I am grateful to Dr. Mark Zoback in the Geophysics department for fruitful conversations and access to petrophysical data. Elnur Aliyev, Jincong He, and Obi Isebor have been particularly helpful in assisting with optimization software. Dr. Jim Erdle with CMG has been an important resource for initial simulation models and software licenses. The SUPRI-B and Smart Fields affiliate companies have provided useful technical feedback.

I also thank my family for their encouragement. Specifically, I want to thank my father for inspiration to pursue graduate study. I would like to also thank Menlo Park Presbyterian Church and their young adult ministry for providing a peaceful respite from academic life and meaningful friendships. My best friend Angela has been an important source of support for me as well. Finally, I would like to acknowledge the financial support of the Stanford Graduate Fellowship for making my time at Stanford possible.

Contents

List of Tables

List of Figures

Chapter 1

Introduction

Natural gas production from US shale reservoirs has increased rapidly in recent years and now accounts for more than 20% of total US gas production. Fig. 1.1, which shows the historical and projected US natural gas production, suggests that shale gas will comprise about half of natural gas production in 2035. Much of the early production was from dry gas fields such as the Barnett Shale in North Texas (Montgomery et al., 2005), but recent industry attention has shifted to gas condensate and light-oil bearing shale formations such as the Eagle Ford of South Texas and the Bakken in North Dakota (Pollastro et al., 2008). Horizontal drilling combined with multistage hydraulic fracturing techniques has been crucial to unlocking both gas and oil from shale reservoirs. These resource plays are characterized by large drilling programs involving hundreds of wells drilled per year.

Given the very low permeability of shale formations, and the fact that the source rock is the reservoir rock, the underlying physics of gas production differs from that associated with more permeable (conventional) reservoirs. Clarkson et al. (2011) and King (2010) provide broad overviews of shale gas production and discuss the relevant physics. This includes matrix flow and flow through fractures of various sizes, gas desorption, non-Darcy effects, and stress-dependent permeability. Flow in hydraulically induced fractures is also crucial to shale gas production. Microseismicity studies have documented the complex nature of the induced fracture network (Mayerhofer et al., 2008; Vermylen and Zoback, 2011). Natural orthogonal fracture networks in

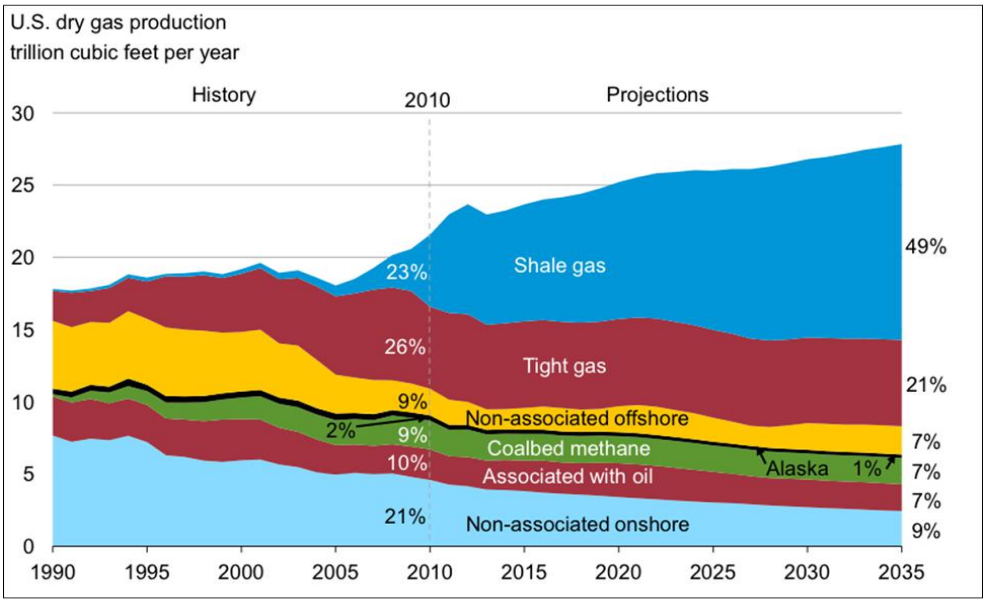

Figure 1.1: Historical and predicted natural gas supply in the United States (EIA, 2012).

shale formations, as described by Engelder et al. (2009), can provide a reference for understanding the induced fractures. Within a shale reservoir, gas may exist both as free gas in pores or as gas adsorbed to the rock (Lu et al., 1995). Depending on the reservoir pore pressure and the details of the desorption process, adsorbed gas may constitute a significant portion of the gas in place. Due to the nanoscale pore structure, molecular phenomena may also impact shale gas production, and some authors have incorporated Knudsen diffusion corrections into Darcy flow equations (Javadpour, 2009).

Numerical reservoir simulation can effectively model discrete fracture networks and the key physical effects, as noted above, that may be important in shale reservoirs. Detailed simulation models have included dual-porosity, dual-permeability and multiple interacting continua (MINC) representations to capture fracture-matrix interactions (Moridis et al., 2010). Discrete fracture models, with the fractures represented using unstructured grids, have also been applied (Cipolla et al., 2011). That particular study involved a detailed workflow that used microseismic data to provide the discrete fracture characterizations. Fracture networks in shale gas reservoirs

have also been represented using refined Cartesian grids and a dual-porosity, dual-permeability framework (Cipolla et al., 2010). This approach enables resolution of pressure transient behavior near the fracture and has been used in conjunction with microseismic imaging to provide properties for the stimulated reservoir volume, or SRV (Mayerhofer et al., 2008).

Computational optimization techniques have been developed for a variety of oil production problems, though they have not been widely applied to shale gas production. Gradient-based procedures to determine optimal well settings (bottom hole pressures or BHPs) have been presented by, e.g., Brouwer and Jansen (2004) and Sarma et al. (2006), while Echeverría Ciaurri et al. (2011) have applied derivative-free pattern search techniques for these problems. Well placement optimization has been considered by a number of investigators, including Yeten et al. (2003) and Onwunalu and Durlofsky (2010), who applied stochastic global search procedures, and Sarma and Chen (2008) and Forouzanfar et al. (2010), who used gradient-based approaches. Computational optimization generally requires hundreds or thousands of flow simulations (the precise number depends on the complexity of the problem and the optimization technique applied), so it is often useful to apply proxy or surrogate models in place of the full-order simulation model. Reduced-order numerical models represent one such proxy, and these approaches have been used with computational optimization procedures (Cardoso and Durlofsky, 2010; Van Doren et al., 2006).

Our goal in this work is to determine the well spacing, well length, and number of fractures for each horizontal well in order to optimize the economics of shale gas production. In our treatment, we first define a "full-physics" simulation model, which represents a high-fidelity description of the reservoir and is viewed as the "reference" model. In our work this model includes highly-resolved fracture networks, dual-porosity, dual-permeability regions, and gas desorption. Our particular example incorporates heterogeneous geology constructed from Barnett Shale well logs using geostatistical techniques. Next, we develop a much simpler (and much faster) reduced-physics surrogate model that can be used for optimization. The parameters that characterize the surrogate model are determined through a tuning procedure that entails "history matching" to the full-physics model. This surrogate model is

periodically retrained during the course of the optimization procedure to maintain quantitative correspondence with the full-physics model. We apply a derivative-free generalized pattern search optimization technique, using the surrogate model, to determine the optimal field development scenario. The overall approach is very general and can accommodate any type of full-physics model, various optimization algorithms, and different strategies for retraining the surrogate model during the course of the optimization.

This thesis proceeds as follows. We first present the full-physics and surrogate models, including the tuning procedure and workflow issues. The optimization problem is then described. Next, results are presented for two field development problems, for which it is shown that the optimized strategies provide net present values that exceed those of the base case developments by 336% and 252%. We conclude with a summary and a discussion of future directions. An alternate procedure and results for idealized two-dimensional cases are presented in an appendix.

Chapter 2

Full-Physics Model and Reduced-Physics Approach

In this chapter, the methods and workflow for the overall procedure are presented. First, a description of the full-physics shale gas simulation is provided. The proxy model and the tuning technique are then presented, followed by the optimization procedure. Finally, the entire workflow is described.

2.1 Full-Physics Simulation Model

2.1.1 Grid and Basic Properties

The full-physics simulation model uses representative properties for the Barnett Shale and is adapted from Cipolla et al. (2010). This approach includes a dual-porosity, dual-permeability treatment, refined grids associated with fractures, non-Darcy flow effects, and gas desorption. The dual permeability, dual porosity treatment differs from the basic dual porosity formulation in that neighboring matrix cells also communicate, as illustrated in Fig. 2.1. The dimensions of the field are $10,600 \text{ ft} \times 5,300 \text{ ft} \times 300 \text{ ft}$, or approximately two adjacent square miles in area. A Cartesian grid of dimensions $106 \times 53 \times 5$ is used in this example. The basic properties for the simulation model are summarized in Table 2.1. Average matrix permeability is 100 nanodarcies

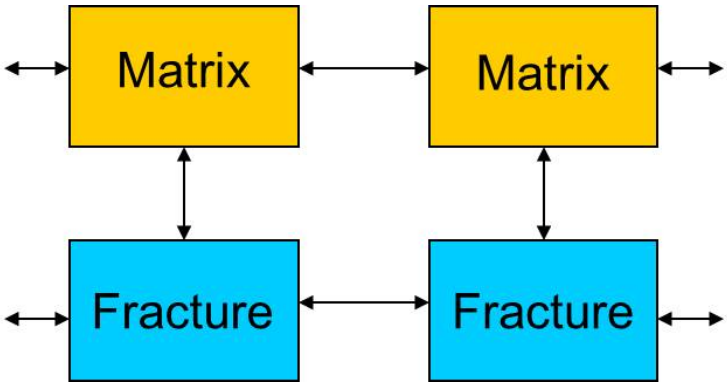

Figure 2.1: Schematic of the dual porosity, dual permeability formulation.

and average porosity is 4.1%. More detail on the geological model can be found in Section 2.1.2.

We use a $7 \times 7 \times 1$ local refinement of the Cartesian grid in the stimulated zone (refinement is applied only in the x and y dimensions). Fracture conductivities (kw, where k is permeability and w is fracture aperture) are 2.0 md-ft for primary fractures and 0.4 md-ft for secondary fractures. Primary fractures are a direct result of the hydraulic stimulation and propagate in the direction of least principal stress (orthogonal to wellbore). Primary fractures are assumed to contain the majority of the proppant material deposited during the stimulation, leading to a higher conductivity than secondary fractures. Both primary and secondary fractures are explicitly modeled with refined-grid cells of thickness 2 ft (k is adjusted in these cells such that kw is preserved). Fractures are aligned with either the x-z or y-z plane and extend over the entire thickness of the reservoir. Fracture half-lengths, x_f, are 500 ft (this and the well length determine the areal extent of the SRV). See Fig. 2.2 for a depiction of a natural fracture network in a Marcellus Shale outcrop along with a corresponding (refined grid) representation of these two orthogonal fracture sets.

The number of grid blocks in the full-physics model depends on the length of the well (which determines the amount of grid refinement), but the typical range for our cases is between 500,000 to 2,000,000 cells. The simulations are time consuming and typical run-times are on the order of 3-10 hours with a single CPU.

(a) Marcellus Shale outcrop (Engelder, 2008)

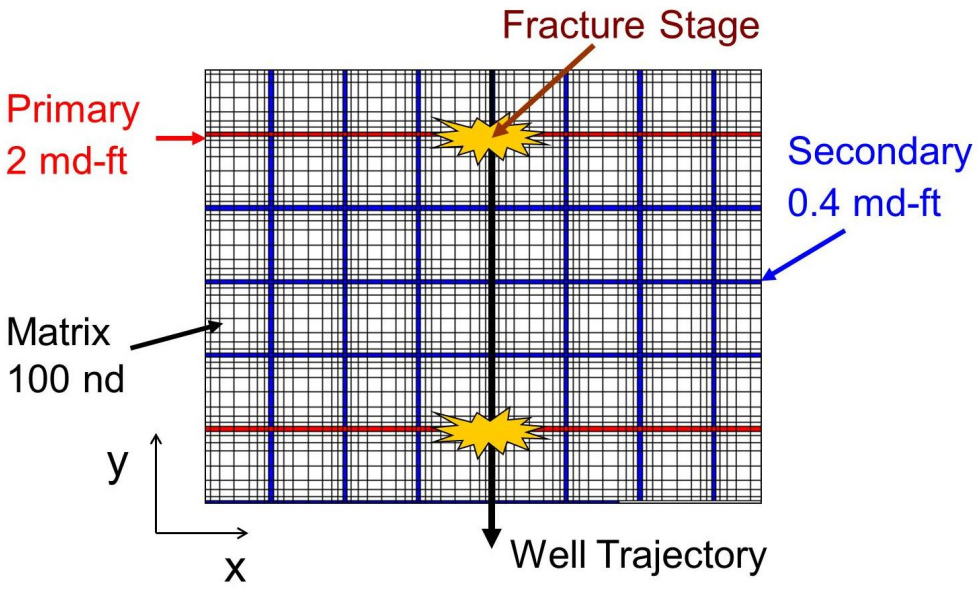

(b) Grid representing fracture network

Figure 2.2: Orthogonal fractures in shales and representation in simulation model.

Table 2.1: Full-physics model properties

Depth	7000 ft
Average Porosity	4.1%
Average Permeability	100 nd
Rock Compressibility	1.25×10^{-5} psi^{-1}
Fracture Half-Length, x_f	500 ft
Grid Dimensions	$106 \times 53 \times 5$
Grid Cell Dimensions	$100 \times 100 \times 60$ ft^3
Grid Refinement (SRV)	$7 \times 7 \times 1$

Desorption is modeled using the Langmuir equation:

$$V_{ads} = \frac{V_L p}{p_L + p}, \tag{2.1}$$

where V_{ads} represents the volume of gas adsorbed in the reservoir rock (scf/ton), p is pressure, and V_L and p_L are termed the Langmuir volume and Langmuir pressure respectively. The Langmuir volume is the maximum adsorption capacity of the rock and the Langmuir pressure is the pressure where V_{ads} is equal to half the Langmuir volume. Frantz et al. (2005) modeled the Barnett Shale with a gas adsorption capacity of 88 scf/ton and a Langmuir pressure of 440 psi. Using these isotherm properties, both free and adsorbed gas can be plotted as a function of pressure, as shown in Fig. 2.3. At an initial pressure of 3800 psi, the gas content in the reservoir is approximately half free gas and half adsorbed gas. As the reservoir pressure drops toward the flowing bottom hole pressure (FBHP) of 1000 psi, this ratio shifts to 75% adsorbed gas. It is evident that gas desorption will not significantly affect gas production until the reservoir has been drawn down substantially below the initial pressure. This behavior is consistent with that observed in previous work for the Barnett Shale (Cipolla et al., 2010), where gas desorption flattened the decline curve after significant production had occurred, but had only a minor effect on cumulative gas production.

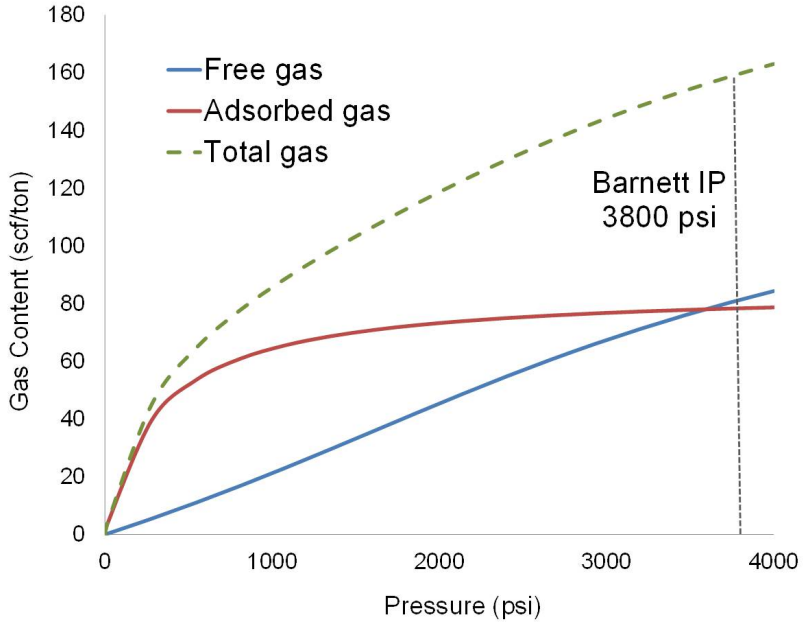

Figure 2.3: Barnett Shale gas content with pressure.

Non-Darcy flow is modeled using the Forchheimer (1901) modification to Darcy's Law:

$$-\nabla p = \frac{\mu}{k}\mathbf{u} + \beta\rho|\mathbf{u}|\mathbf{u}, \tag{2.2}$$

where $\mathbf{u}$ Darcy is velocity, μ is viscosity, permeability k is taken to be isotropic, β is the Forchheimer correction, and ρ is phase density. Darcy's law is recovered for $\beta = 0$. For flow in many different porous media, Evans and Civan (1994) proposed the following equation for β:

$$\beta = \frac{1.485 \times 10^9}{\phi k^{1.021}}, \tag{2.3}$$

where ϕ is porosity. Since the fractures have been "effectivized" to 2.0 ft grid cells from their assumed physical width of 0.001 ft (this effectivization preserves kw), a correction factor, as described by Rubin (2010), is applied to the grid cells representing fractures.

As indicated earlier, for the purposes of this work, the full-physics simulations are treated as reference solutions. In our full-physics representation, many key effects are included, but others, such as coupled geomechanics, are not. This is not a limitation

of the general procedure, as the full-physics model can include whatever effects are deemed necessary for the problem under study.

2.1.2 Geologic Model Construction

Petrophysical log data from five wells in the Barnett Shale were used together with geostatistical techniques to build a simple geological model of the reservoir that can be used for flow simulation. The well logs considered in this analysis are the gamma ray values for five horizontal wells along with density-porosity data from a single well in the set. Yang and Alpin (2010) developed a correlation for mudstone and shale permeability as a function of porosity and clay content. In order to utilize this correlation, clay content must be deduced from the gamma ray logs. Our procedure is as follows. First, using sequential Gaussian simulation (SGS), a 3D grid was populated with gamma ray values. SGS is a commonly used geostatistical technique that provides a heterogeneous field honoring the variogram and hard (measured) data (Deutsch and Journel, 1992). The model at this stage contains grid blocks that are 100 ft $\times$ 100 ft $\times$ 60 ft, resulting in a total of about 28,000 blocks.

The amount of clay in a reservoir can be correlated to gamma ray readings because radioactive elements (potassium, thorium, uranium) are primarily found in the clays. Clay content is typically calculated through an empirical formula:

$$C_{clay} = \frac{GR_{log} - GR_{min}}{GR_{max} - GR_{min}} C_{clay,max}, \tag{2.4}$$

where GR_{max} and GR_{min} are the maximum and minimum gamma ray values on the log sustained over a minimum length interval to eliminate noise (Darling, 2005). The quantity $C_{clay,max}$ refers to the maximum amount of clay found in the reservoir, and is typically interpreted from reservoir cores or local geology. For this study, $C_{clay,max}$ was taken as 60% and GR_{min} and GR_{max} were taken from the logs as 30 and 300 API units respectively. This is consistent with literature values, as Kuuskraa et al. (1998) reported gamma ray values up to 400 API units and Jarvie et al. (2007) described highly variable clay content from 0-65% in the Barnett Shale. Fig. 2.4 displays a histogram of the calculated clay content, where most of the values fall between 20%

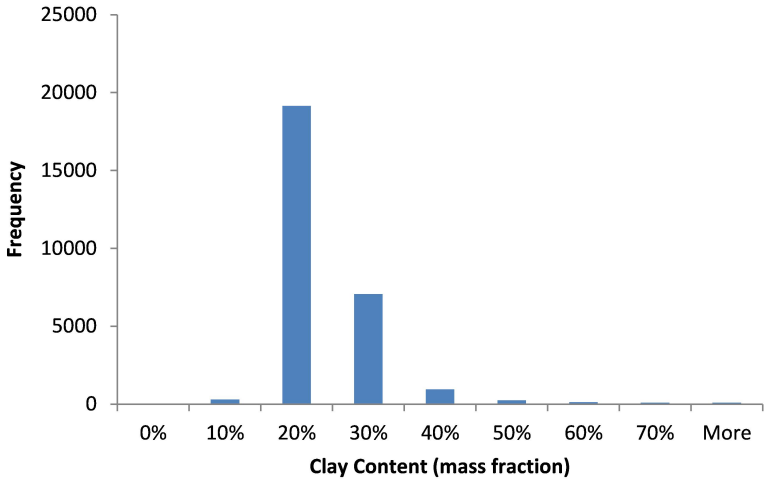

Figure 2.4: Histogram of reservoir clay content.

and 40% clay by mass. This is consistent with literature values, where the Barnett Shale clay content was reported as between 10-50% (Bruner and Smosna, 2011).

Porosity data was inferred from a density log of the vertical section of a single well in the reservoir. As can be seen from Fig. 2.5, the porosity log exhibited a significant amount of noise; for this reason the log was averaged over 60 ft intervals for modeling purposes. Density porosity is calculated from the following equation:

$$\phi_d = \frac{\rho_m - \rho_{log}}{\rho_m - \rho_{fluid}}, \tag{2.5}$$

where ρ_m and ρ_{fluid} are the densities of the rock matrix (zero-porosity) and the reservoir fluid (water in this case) respectively. In this case, the matrix density for the well log was assumed to be 2.71 g/cm^3, corresponding to the density of limestone, which is prevalent in the Fort Worth Basin mineralogy. The reservoir fluid was taken to be water with a density of 1 g/cm^3. The average porosity from the well log, interpreted in this manner, was 12.8%, which is much higher than reported values of 3-6% in literature.

This discrepancy may result because the matrix density is assumed constant over the well log, even though the well passes through many different formations. This

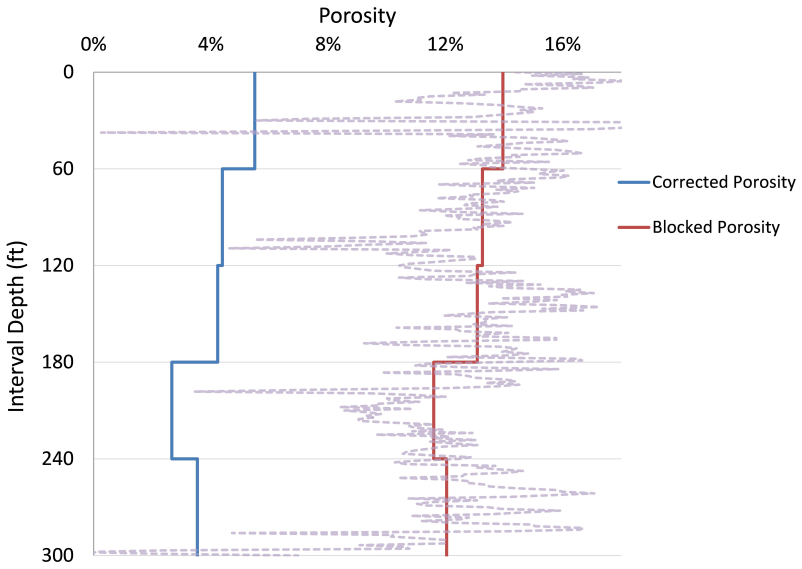

Figure 2.5: Vertical density-porosity log and corrected values.

can lead to errors in the characterization of the reservoir. One source of error in zones with high organic content is due to kerogen's lower density of about 1.7 g/cm^3 (Ward, 2010). To address this issue, the matrix density for the Barnett Shale was adjusted to 2.55 g/cm^3, which led to an average porosity value of 4.1%. Literature values report bulk density between 2.5-2.6 g/cm^3 and porosity typically between 3-6% (Jacobi et al., 2008). This step leads to the "Corrected Porosity" values displayed in Fig. 2.5. Adjusting matrix density in density porosity calculations is common industry practice, see for example Zhao et al. (2007). Because porosity was derived from a vertical well, the porosity model of this reservoir will be strictly layered, with constant values for each vertical layer.

Once the values of porosity and clay content have been established over the geologic grid, the remaining step is to assign permeability values using a modified version of the Yang and Alpin (2010) equation. This correlation was derived empirically by curve fitting published data from a variety of mudstone and shale samples. The correlation uses clay content and porosity to determine permeability. This correlation was normalized in our work to provide a mean permeability of 100 nanodarcies over the entire reservoir, consistent with values reported by Bruner and Smosna (2011). A

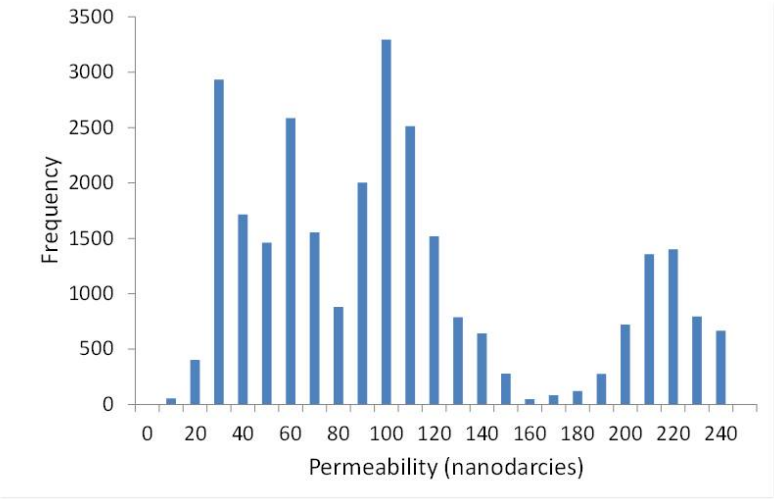

Figure 2.6: Histogram of matrix permeability for the 3D model.

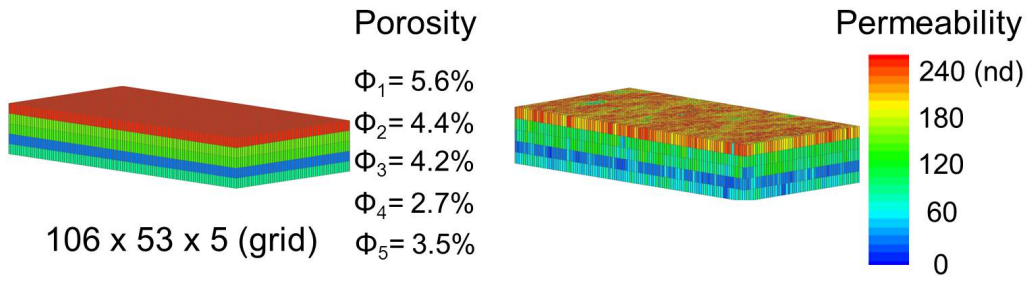

Figure 2.7: 3D model porosity (left) and permeability (right).

histogram of the calculated permeability values (Fig. 2.6) shows a multi-modal distribution. The layer with the highest porosity accounts for most of the permeability values above 200 nanodarcies.

Fig. 2.7 displays the final geological (porosity and permeability) model, where porosity is strictly layered and permeability varies in x, y, and z. As mentioned above, the high porosity top layer contains the highest permeability values. There are approximately two orders of magnitude variation in matrix permeability. This model defines the underlying geology in the flow simulations used in this study.

2.2 Surrogate Model and Tuning Procedure

The reduced-physics surrogate is a simplified model that treats fewer physical effects and contains fewer grid blocks than the full-physics model. As a result, simulation runs using this model require much less computation time. The parameters associated with this model are determined by a tuning procedure using full-physics models as reference solutions.

Some amount of numerical experimentation must be performed to determine the level of physics and grid resolution required for the reduced-physics model. Our investigations showed that single-porosity models, without desorption, non-Darcy effects or local grid refinement but with tuned multipliers for permeability and porosity in the stimulated zone (designated M_k and M_ϕ), could provide results in close agreement with the full-physics model. Property multipliers are constant values that act on every (i,j,k) grid block within the stimulated zone. Multipliers preserve local heterogeneity because the property in the stimulated zone will be a function of both the original matrix property and the property multiplier:

$$\begin{aligned} (\phi_s)_{i,j,k} &= (\phi_m)_{i,j,k} \times M_\phi, \\ (k_s)_{i,j,k} &= (k_m)_{i,j,k} \times M_k, \end{aligned} \tag{2.6}$$

where subscript m indicates the matrix property of a grid block in the full-physics model and subscript s denotes the property in the stimulated zone of the surrogate model. Permeability and porosity values outside the stimulated zone remain identical to those in the full-physics model. Instead of explicitly modeling fractures, each fracture in the reduced-physics model is represented through a completion along the wellbore in the stimulated region. The reduced-physics model, shown in Fig. 2.8, thus contains at least a factor of 20 fewer grid blocks than a typical full-physics model.

The determination of M_k and M_ϕ is accomplished using a procedure akin to history matching, but instead of using historical data we use the gas production of the full-physics model. Specifically, we determine the surrogate-model parameters such that the difference in predictions between the full-physics and surrogate models is minimized for a particular set of wells (multiple well configurations can also be

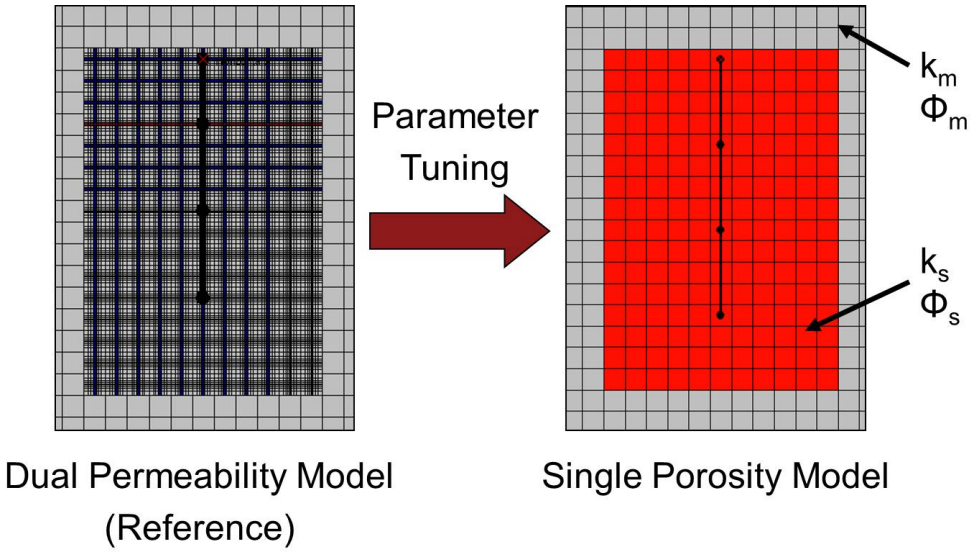

Figure 2.8: Full-physics (left) and surrogate (right) simulation models.

considered). The quantity we seek to minimize, denoted by J, is defined as:

$$J = \sum_{n=1}^{N} \left(q^n_{ref} - q^n_{surr}\right)^2 \; e^{-it_n}, \tag{2.7}$$

where n indicates the time step and N indicates the maximum number of time steps in the simulation, q^n_{ref} and q^n_{surr} are the field gas production rates for the full physics and surrogate models, and i is an interest rate which is used to discount gas production. Note that the particular form of J should be chosen consistent with the actual production optimization problem (e.g., if discounting is not used we would set $i = 0$).

The optimization problem we solve for the tuning of the surrogate model is: Find the $(M_k,\ M_\phi)$ that minimize J in Eq. 2.7. We solve this problem using a generalized pattern search (GPS) algorithm (Kolda et al., 2003). GPS is a stencil-based direct search method that moves systematically through the $(M_k,\ M_\phi)$ parameter space. A two-dimensional GPS is depicted in Fig. 2.9. The red star in the first frame indicates the local minimum and the curves are contours of the objective function. The stencil at iteration $\nu + 1$ is centered on the best point found through iteration ν. All points on the stencil, five in this case, are then evaluated at iteration $\nu + 1$ (results can

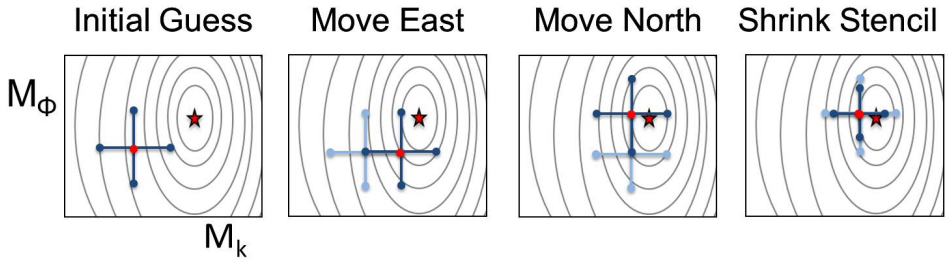

Figure 2.9: Illustration of generalized pattern search optimizer for surrogate tuning.

be saved to avoid re-running cases that have already been simulated). The stencil is then shifted to the best point and the procedure continues. When the search no longer provides improved values, the stencil size is reduced (last frame in Fig. 2.9). Convergence occurs when no improvement in the solution is attained and the stencil size has reached its user-specified minimum. GPS is a local optimizer, but some amount of global exploration can be achieved by choosing a sufficiently large initial stencil size.

The tuned surrogate model can now be used to evaluate many different well designs in order to optimize the economics of shale gas reservoirs. In this work, the surrogate model is initially trained to a base case field design. During the course of the field development optimization, this field design will change and the surrogate model will need to be retrained. This is accomplished by periodically computing an updated M_k and M_ϕ, as will be discussed in Section 2.4.

2.3 Field Development Optimization

After the tuning process, the reduced-physics model can be expected to provide simulation results that are similar to those of the full-physics model (at least for well configurations that are similar to those used for the tuning), so it can be used to evaluate field development scenarios. A number of decisions are generally required for the development of shale resources including the determination of the number, location and length of new wells, and the number of hydraulic fractures completed in each

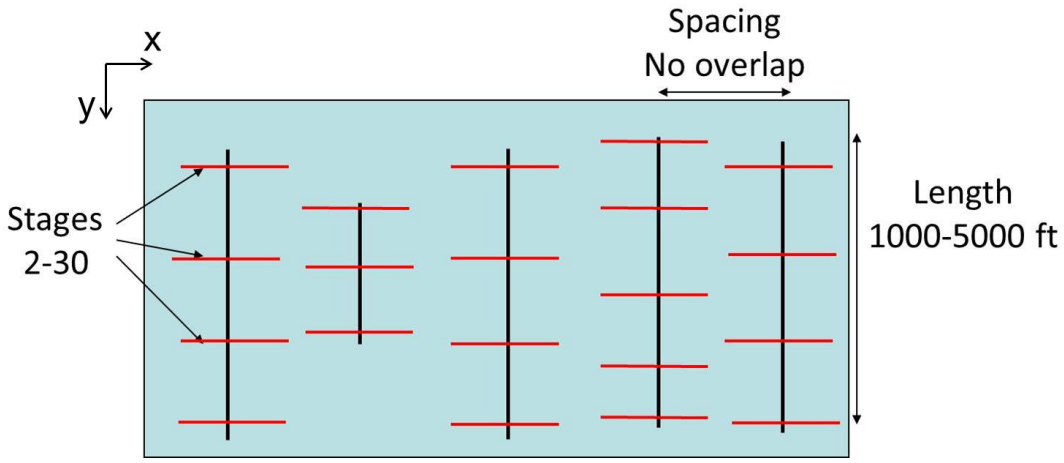

Figure 2.10: Possible wells and fractures for field development optimization.

well. Additional issues involving the detailed completion design must also be considered. Computational optimization procedures can efficiently sample the search space defined by these many decision parameters and associated constraints to determine the most economic field development plan.

In this work, all wells are taken to be horizontal and to extend in the y-direction. We specify the total number of wells N_w. The decision variables determined in the optimization are the x-locations of the heel of each well (x_i), the length of each well (L_i), and the number of fracture stages in each well ($N_{f,i}$). Each well is centered in the y-direction and completed in the middle layer of the model so its location is determined solely by the two variables x_i and L_i. Fracture half-length, x_f, is fixed at 500 ft in our models. Fracture stages are spaced equally along the length of the well as shown in Fig. 2.10. Wells must be separated by a minimum distance of two fracture half-lengths, $2x_f$. There are a total of $3N_w$ decision variables. The bounds (minimum and maximum) associated with each of these variables are provided in Table 2.2. More decision variables could of course be considered, but this would increase the complexity of the optimization problem.

The objective function we seek to optimize is the net present value (NPV) of the field development, which is the sum of the discounted cash flows (DCF) minus the

capital expenditures, C_{capex}:

$$NPV = \sum_{n=1}^{N} DCF_n - C_{capex}. \tag{2.8}$$

For this calculation, a cost function was constructed from publically available data. An example cost function for a shale gas well was given by Williams-Kovacs and Clarkson (2011) and a modified version of this is used in this work. Discounted cash flow is given by:

$$DCF_n = (1 - T)\left[q_n G(1 - R) - C_{LOE}\right] e^{-it_n}, \tag{2.9}$$

where q_n is production over the time step, G is the gas price, R is royalty payment, and T is tax rate. In this work, rates of 15% and 30% were used for royalty and tax, respectively. A lease operating cost, C_{LOE}, of \$150/day is also incorporated. Note that continuous economic discounting is used.

The capital expenditure for the development is an upfront cost composed of three components – the leasing cost, the drilling cost, and the completion cost:

$$C_{capex} = C_{lease} + C_{drill} + C_{frac}. \tag{2.10}$$

The leasing cost is set at \$1.28M for the field, or \$1000/acre. This cost is independent of the well design and does not impact the solution to the optimization problem. The cost to drill each well is \$250 per foot of measured depth (vertical depth plus horizontal length for simplicity). Completion costs are specified as \$250,000 per fracture stage. These costs were inferred from recent corporate presentations and industry articles (Cowan, 2011; Marsh et al., 2011). Depreciation is not included in these calculations. A summary of the costs is given in Table 2.3.

We again use GPS to determine the field development parameters (x_i, $N_{f,i}$, L_i) that maximize NPV. The dimension of the search space is now 15, which is much larger than the search space for tuning the surrogate model, but the generalization of GPS to higher dimensions is straightforward. This optimization does, however, require

Table 2.2: Field development optimization constraints

Variable	**Constraints**
Well Heel Location, x_i	$x_i - x_{i-1} \geq 2x_f$
Fractures, $N_{f,i}$	2–30
Horizontal Length, L_i	1000–5000 ft

Table 2.3: Economic model parameters

Gas Price	\$3.50/mcf
Lease	\$1.28M
Drilling	\$250/ft
Completion	\$250,000/stage
Operating	\$150/day
Royalty	15%
Tax	30%

much more computation, because the number of function evaluations (simulations of the surrogate model in this case) per GPS iteration scales with the dimension of the search space.

2.4 Overall Tuning and Optimization Workflow

The workflow described above entails first defining and tuning a surrogate model. Next, this surrogate model is used for optimizing field development. During the course of the optimization procedure, it may be necessary to retrain the surrogate model to ensure that its accuracy is maintained. In our work, this "retraining" is applied after the optimization procedure has performed a specified number of function evaluations (simulations of the surrogate model). At this point, a full-physics simulation is performed using the current best configuration of wells and fractures. This serves as the reference model for retraining the surrogate. A flowchart of the entire workflow is shown in Fig. 2.11.

Each time a full-physics simulation is performed, the NPV is also calculated. If, at some point, the NPV for the current full-physics model is not higher than that for the previous full-physics model, the optimization proceeds from the previous trained

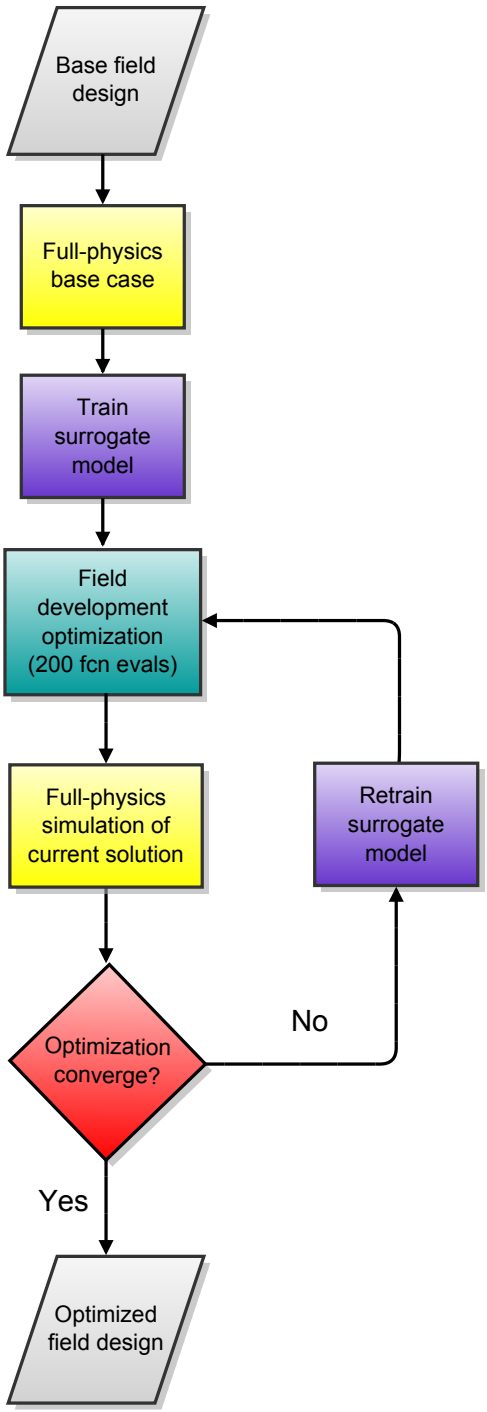

Figure 2.11: Field development optimization with surrogate retraining algorithm.

surrogate. Retraining is then applied after a smaller number of function evaluations.

There are several variants of this basic workflow that could be applied, and some of these have been tested in this work. For example, the surrogate model could be tuned once, for a range of well designs, and then left unchanged during the optimization. Such an approach, discussed in Appendix A, was used for idealized two-dimensional models. Additionally, following convergence of the optimization using the surrogate model, the full-physics model could be used for further optimization. This approach could be time-consuming, but it will be much more efficient than direct optimization using the full-physics model.

Chapter 3

Results and Discussion

In this section, we present results for the surrogate tuning procedure and for two example optimization problems involving different economic scenarios. The field developments involve five horizontal wells placed parallel to the y-axis. As described in Chapter 2, the full-physics simulations include a dual-porosity, dual-permeability formulation, explicit fractures described by locally refined grids, non-Darcy flow effects and gas desorption. All simulations in this work are performed using CMG's IMEX black-oil simulator (CMG, 2010).

A list of properties and correlations used for the simulations is given in Table 3.1. Well BHPs are set to 1000 psi, except at very early times where a maximum surface gas rate constraint of 10 MMscfd may take effect. The well radius, r_w, is 0.125 ft reflecting the common use of tubing in gas wells. The initial reservoir pressure is 3800 psi. A method developed by Seidle and Arri (1990) for including Langmuir desorption effects in black-oil simulators was incorporated in this work. The viscosity of water was assumed to be constant. Gas specific gravity, γ_g, was taken as 0.71 at stock tank conditions (14.7 psia, 60 °F). Relative permeability curves with Corey exponents of 2.0 were used to model both water and gas phases. Hysteresis was not considered. Initial and irreducible water saturation are both equal to 30%, leading to no water production in this model.

Table 3.1: Reservoir simulation model properties

PVT Properties	
p_i	3800 psi
T	180 °F
μ_w	0.37 cP
μ_g	Gonzalez and Lee (1968)
B_w	1.03
B_g	Standing and Katz (1942)
γ_g	0.71
Langmuir Volume	88 scf/ton
Langmuir Pressure	440 psi
Relative Permeability Model	
$S_{w,i}$	0.3
$S_{w,min}$	0.3
$S_{g,r}$	0.02
C_w	2
C_g	2
Well Description	
r_w	0.125 ft
Geometric Factor	0.37
Minimum BHP	1000 psi

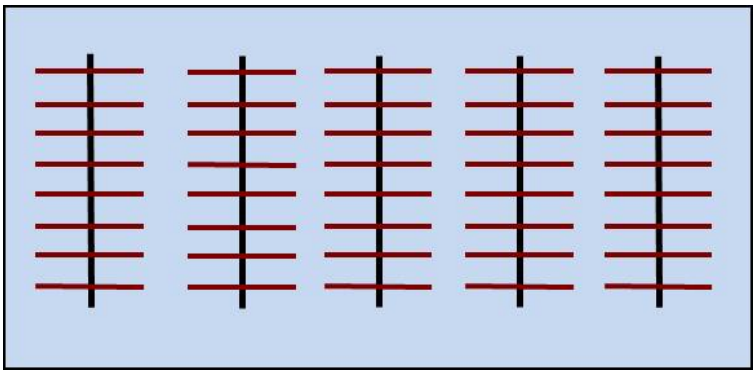

Figure 3.1: Base case field design.

3.1 Results from Tuning Procedure

As described in Section 2.2, the surrogate model is initially tuned to a base case field design. This design contains five evenly spaced wells, with 3000 ft laterals and eight fracture stages per well, as shown in Fig. 3.1. The minimization problem defined earlier is then solved using GPS to provide M_ϕ and M_k. Because of the nature of the decline curve and the effect of discounting, only ten years of production are simulated. Monthly field production is recorded, for a total of 120 data points from each run.

The progression of the GPS tuning is shown in Fig. 3.2. After 98 function evaluations, the mismatch between the full-physics and surrogate models was reduced to less than 2% of its initial value. The initial and optimized SRV properties, along with the optimization constraints, are displayed in Table 3.2. The stimulated zone permeability was multiplied by a factor of 195, while the increase in porosity was much less significant. The increase in permeability accounts for the fracture network, which is no longer modeled explicitly but contained within single porosity grid cells. On the other hand, the increase in porosity within the SRV largely accounts for gas desorption effects, which are not explicitly included in the surrogate models.

Tuning results for the base case scenario are shown in Fig. 3.3. The solid blue line represents gas production from the full-physics model, which serves as the reference data for the tuning procedure (q_{ref} in Eq. 2.7). The dashed lines represent the surrogate model response for both the initial and tuned porosity multipliers. It is apparent that the tuning procedure is able to provide a surrogate model that gives

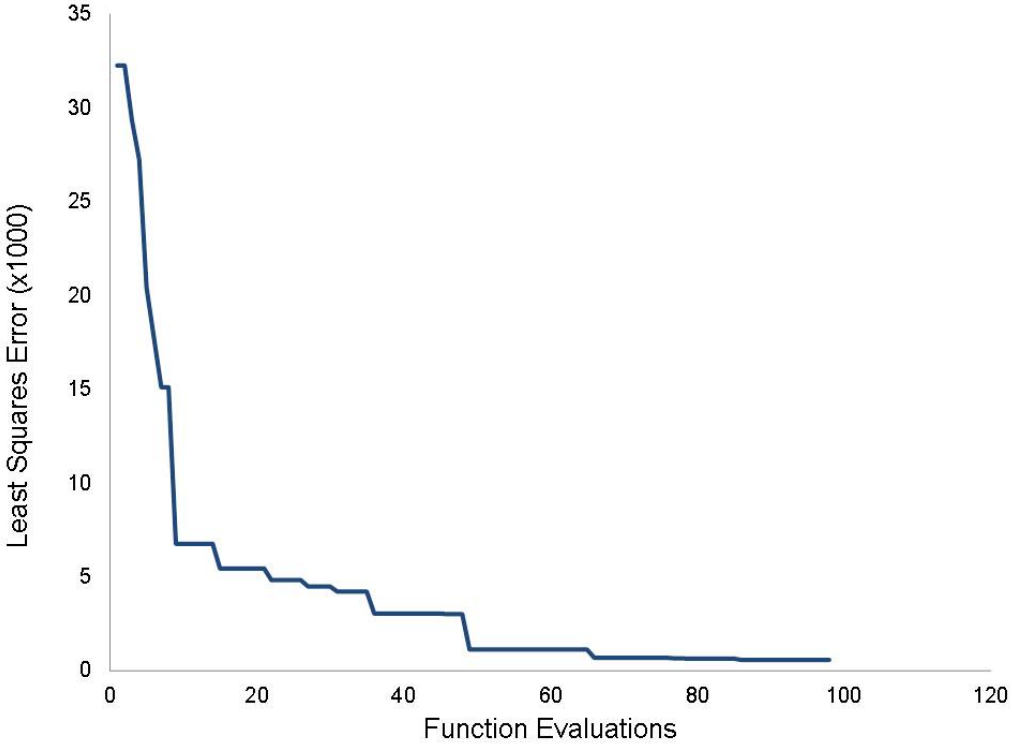

Figure 3.2: Optimization performance for tuning of the surrogate model.

Table 3.2: Initial and tuned stimulated zone property multipliers

Property Multiplier		**Initial**	**Optimized**
M_ϕ	(0.5 - 3)	1	1.20
M_k	(50 - 300)	100	195

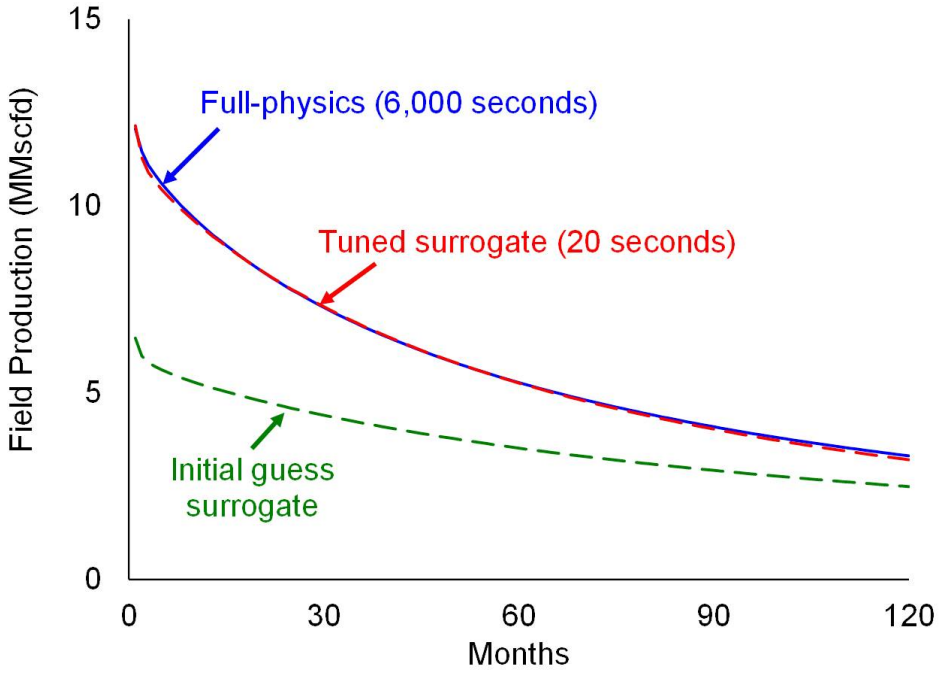

Figure 3.3: Tuning results for base case field design.

results in close agreement to the reference full-physics model.

A comparison of production from two individual wells (Well B and Well D) is shown in Fig. 3.4. The wells are labeled from left to right in the areal field design. These results display slightly more error than the field-wide results in Fig. 3.3, though it is nonetheless evident that the surrogate model also provides accurate well-by-well production rates.

These simulations were performed on a single CPU machine with 2 GB of memory. The computational demand for the full-physics simulations is proportional to the total number of grid cells, which depends on the length of the horizontal well and the number of fractures. The surrogate models do not utilize refined grids, so their CPU expense does not vary based on the well design. The tuned surrogate model runs about 300 times faster than the full-physics model for this well design. For this example, depending on the specific well/fracture configuration, we observe speed-ups ranging from about 200 to 700.

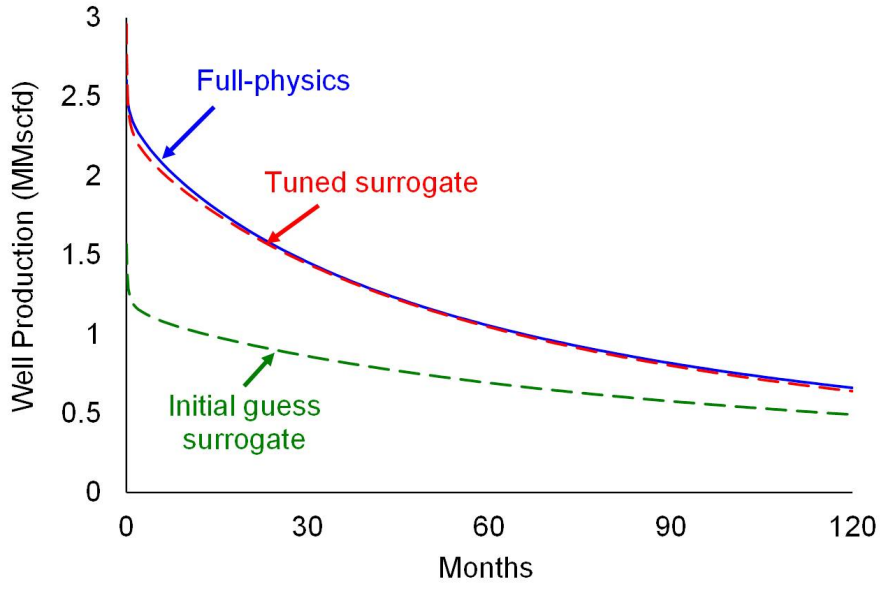

(a) Well B

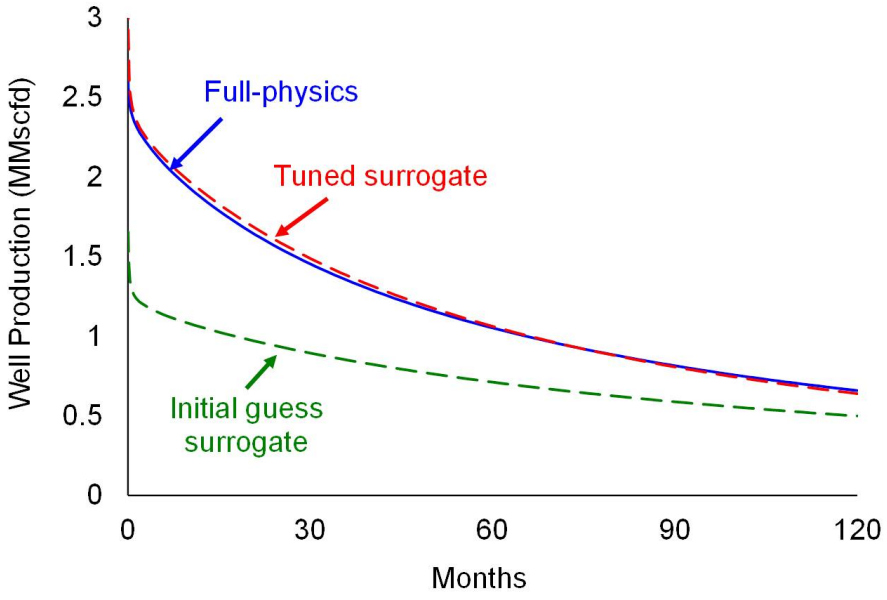

(b) Well D

Figure 3.4: Well production comparison for the base case field design.

The pressure fields associated with the full-physics and surrogte models at various times are also of interest. In Fig. 3.5, pressure profiles of the middle reservoir layer with the base case well design are compared. As shown in Fig. 3.5(a), the pressure in the fracture network of the full-physics model decreases at early time. The surrogate model does not contain an explicitly modeled fracture network and displays more complete reservoir drainage near the well. After ten years of production, a comparison of the pressure profiles does not reveal any major differences, as evident in Fig. 3.5(b). At early times, free gas production from the fracture network is dominant, but at later times more gas is produced from the low permeability matrix within the stimulated zone. The surrogate model effectively captures both of these effects through properly tuned M_k and M_ϕ.

3.2 Field Development Optimization Results

We now present results for field development optimization. The surrogate model is initially tuned to the base case well design and then periodically retrained during the course of the optimization. In this work, it was found that retraining the surrogate model every 200 function evaluations led to acceptable solution performance.

The initial guess for the optimization includes five evenly spaced horizontal wells, 3000 ft in length, with eight fracture stages (this is the base case described in Section 3.1). The performance of the GPS optimization is shown in Fig. 3.6. The blue curve displays the optimization performance using the surrogate model, while the stars depict results using the full-physics model during the optimization. The yellow star represents a verification of the accuracy of the surrogate model for the optimum configuration at the end of the optimization. Red stars indicate the periodic full-physics training or retraining runs used to calibrate the surrogate model. There is clearly very close agreement between the two models for the optimized configuration (see Table 3.3 for a detailed comparison), which demonstrates the efficacy of the surrogate modeling procedure.

In terms of the actual optimization results, after nearly 700 function evaluations the optimized NPV is more than a factor of three greater than the base-case NPV. Five

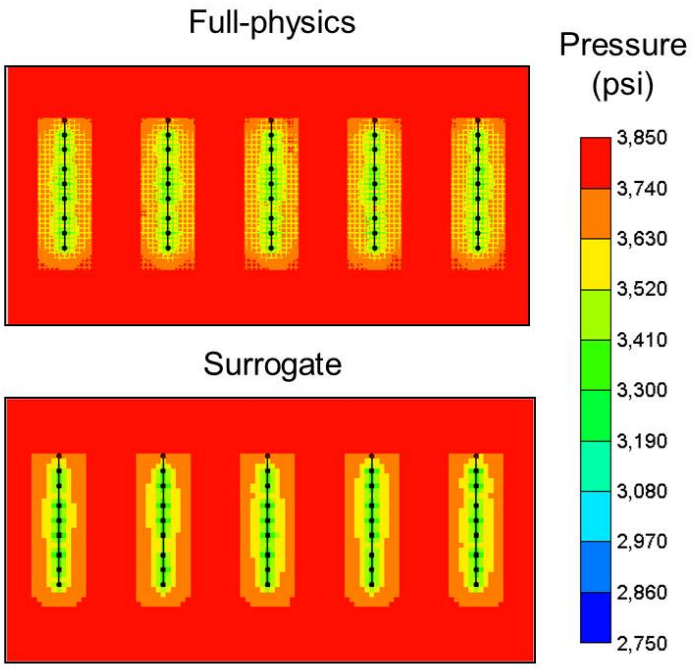

(a) Six months

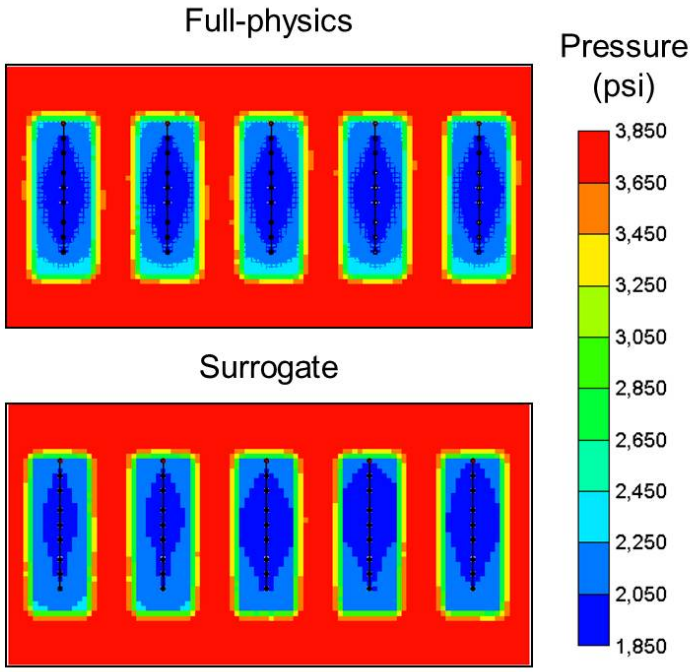

(b) Ten years

Figure 3.5: Pressure profiles at six months and ten years.

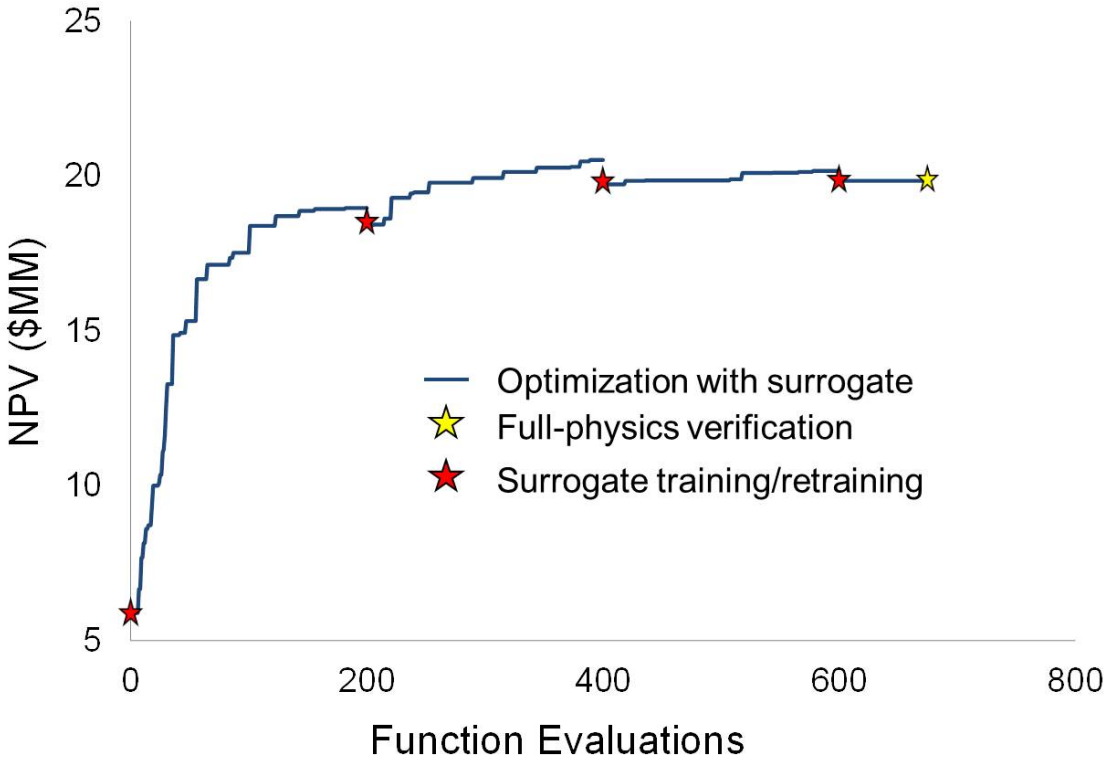

Figure 3.6: Field development optimization performance.

full-physics simulations were required during the course of the optimization (four runs for training and a final verification). The surrogate-model simulations associated with the field development optimization require less CPU time than a single full-physics simulation. This means that the use of surrogate models leads to a speed-up factor of over 100 compared to optimizing the field using the full-physics model.

The surrogate model was trained four times during the course of the optimization. Fig. 3.7 displays the best field design after 200 function evaluations. The optimizer has lengthened the horizontal sections and added fracture stages compared to the wells in the base case. A full-physics simulation of this field design is performed and used for retraining the surrogate model. Fig. 3.8 shows the progress of the GPS optimization for this retraining. The initial error is much smaller initially in this case, at about 3,000 compared to 32,000 for the initial tuning shown in Fig. 3.2. Initial

Table 3.3: NPV for initial and converged solutions

	Surrogate	Full-Physics	Error
Initial ($MM)	5.89	5.93	0.7%
Converged ($MM)	19.84	19.93	0.5%
Change	337%	336%	

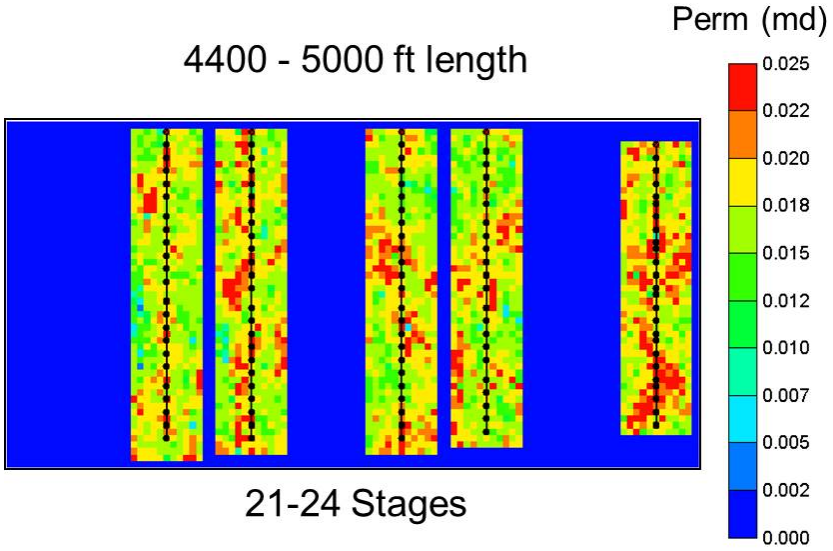

Figure 3.7: Best field design after 200 function evaluations.

and tuned surrogate production responses are compared to the reference full-physics results in Fig. 3.9. The initial surrogate shows slightly higher gas production at early times while the tuned surrogate matches the reference production more closely at these times.

Relatively small changes in (M_ϕ, M_k) take place after the surrogate model is initially tuned, as shown in Table 3.4. The porosity multiplier increases slightly (2%) as the optimization progresses, while the permeability multiplier declines by 8%. The fact that M_ϕ and M_k change only slightly during the course of the optimization is encouraging and indicates that the surrogate model can be expected to remain accurate over a range of well and fracture configurations.

Areal views of the field development plans for the base case and the optimized solution are shown in Fig. 3.10. The optimized well lengths are the maximum allowed

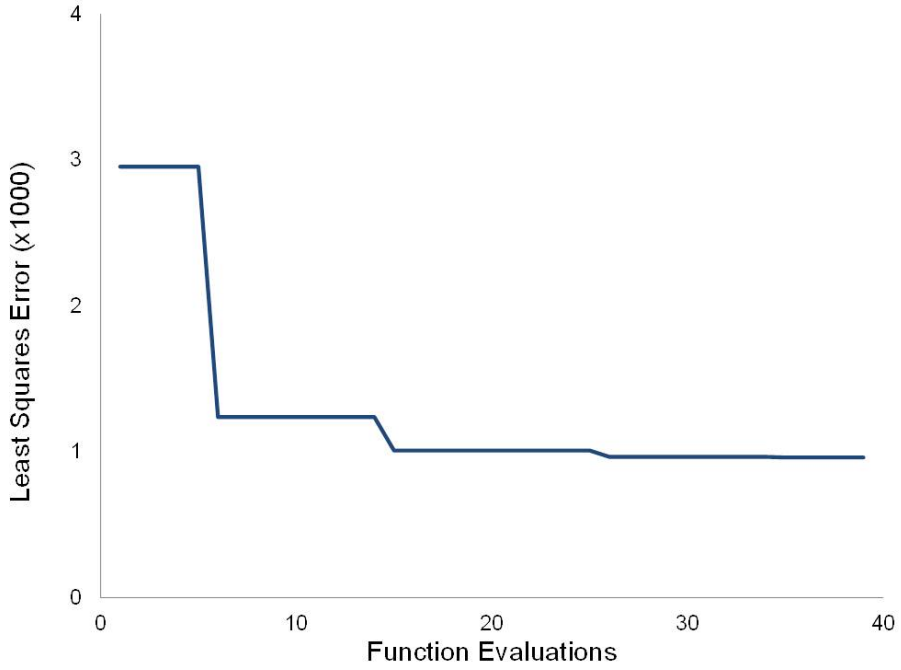

Figure 3.8: Retraining performance after 200 function evaluations.

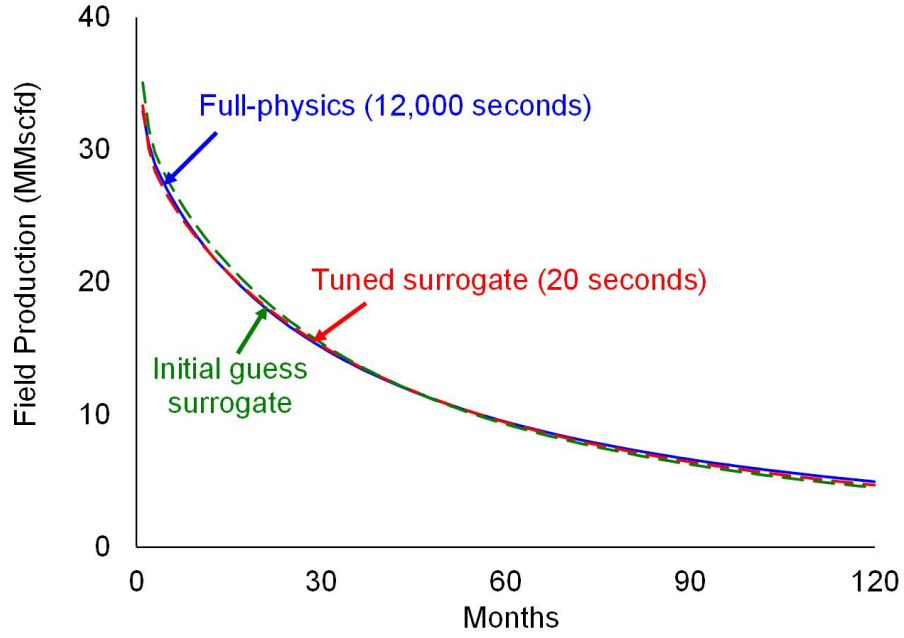

Figure 3.9: Production responses before and after retraining.

Table 3.4: Stimulated zone property multipliers used in the optimization

	M_ϕ	M_k
Initial Tuning	1.206	194.3
200 Iterations	1.229	187.6
400 Iterations	1.233	185.4
600 Iterations	1.231	178.9

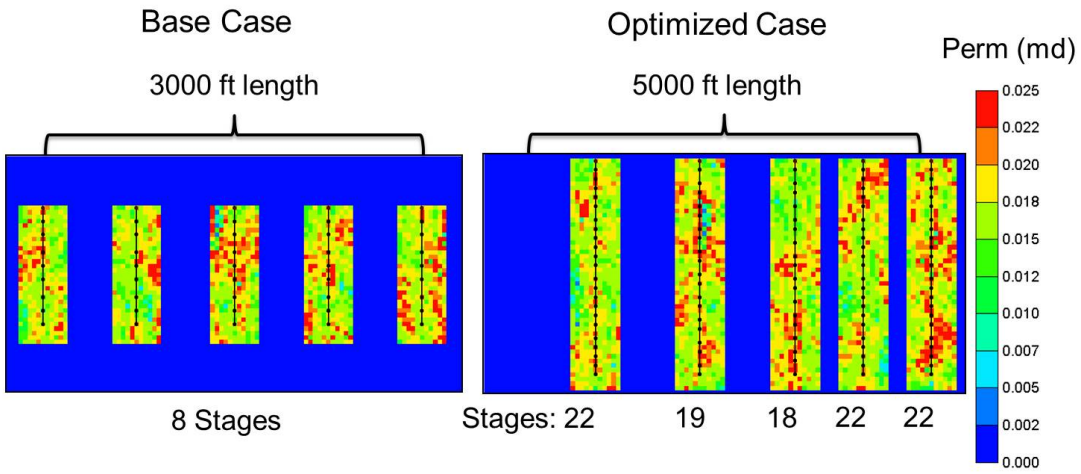

Figure 3.10: Base case and optimized field design.

(5000 ft), though the wells include a variable number of fracture stages (from 18 to 22 depending on reservoir quality). This is consistent with current practice in shale reservoirs, where the typical well is completed with between 10 and 20 stages (Thompson et al., 2011). These results demonstrate that tailoring the number of fracture stages to reservoir quality can improve economic returns in the development of shale resources.

3.2.1 Aggressive Development Case

To demonstrate the adaptability of the workflow to variable economic conditions, a second example involving higher gas prices and capital costs was considered. In this example, the price of natural gas is doubled (to \$7.00/mcf) and well drilling and completion costs experience an increase of 50%. A summary of costs in this example

Table 3.5: Economic model parameters for aggressive development case

Gas Price	\$7.00/mcf
Lease	\$1.28M
Drilling	\$375/ft
Completion	\$375,000/stage
Operating	\$150/day
Royalty	15%
Tax	30%

is given in Table 3.5. Average capital expenditures in this case range from \$7-15 MM per well. This scenario is intended to represent an "aggressive development," where a relatively high gas price spurs activity and increases competition for drilling and completion services.

The base case field design is equivalent to that used in the previous example, with equally spaced wells with 3000 ft laterals and eight fracture stages apiece. Fig. 3.11 displays the performance of the optimization procedure along with the four full-physics solutions used to train and verify the surrogate model. The surrogate model and full-physics solutions again show excellent agreement, with less than 1% error for both the base case and optimized field designs, as indicated in Table 3.6. In this example, the field NPV was increased by a factor of 2.5 to nearly \$65 MM during the optimization. This is more than three times higher than the NPV found in the previous example. It is evident that the increase in gas price more than compensates for the rise in service costs in this case.

The optimized field designs for both examples are displayed in Fig. 3.12. Under aggressive economic conditions, it is again optimal to extend the horizontal wells to the maximum allowable length (5000 ft). With the drilling cost a function of measured depth, there is an incentive to maximize reservoir contact by extending the horizontal section to recover the cost of drilling the 7000 ft vertical section. This result is underscored by the recent industry trend toward longer horizontal well sections and multilateral wells (Durst and Vento, 2012). The average number of fracture stages per well rose to 25 compared to 21 in the previous example. The algorithm thus balances the marginal cost of additional fracture stages (\$375,000) with the positive

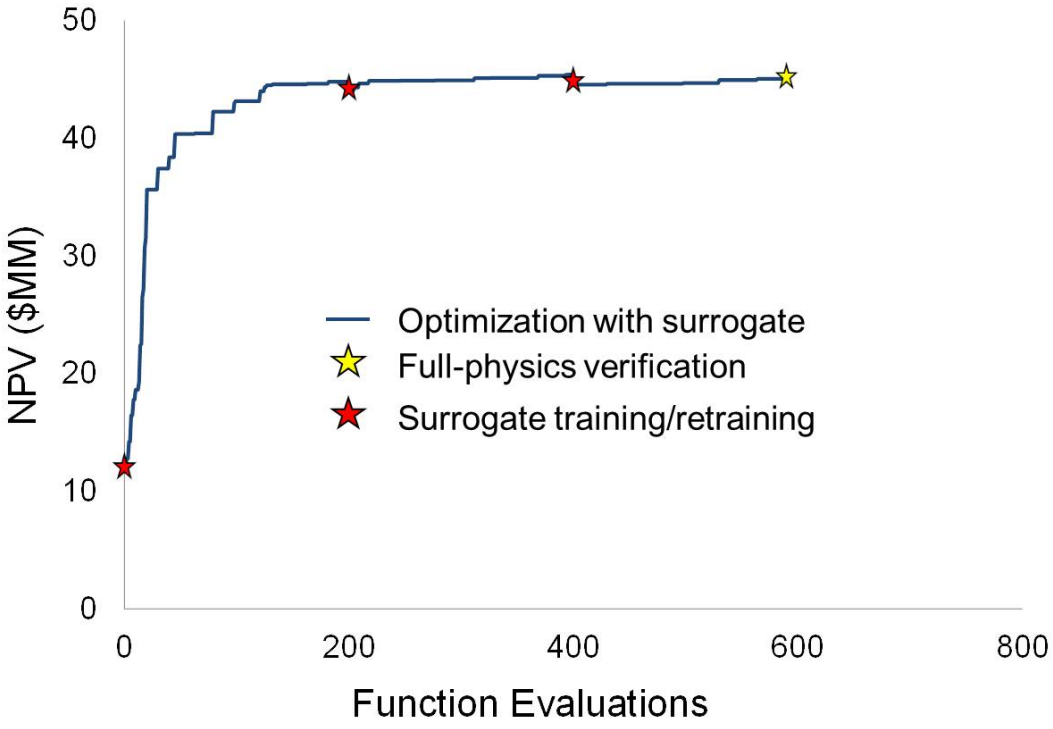

Figure 3.11: Optimization performance for the "aggressive development" case.

Table 3.6: Initial and converged NPV for aggressive development example

	Surrogate	Full-Physics	Error
Initial ($MM)	25.56	25.60	0.2%
Converged ($MM)	64.79	64.63	0.2%
Change	253%	252%	

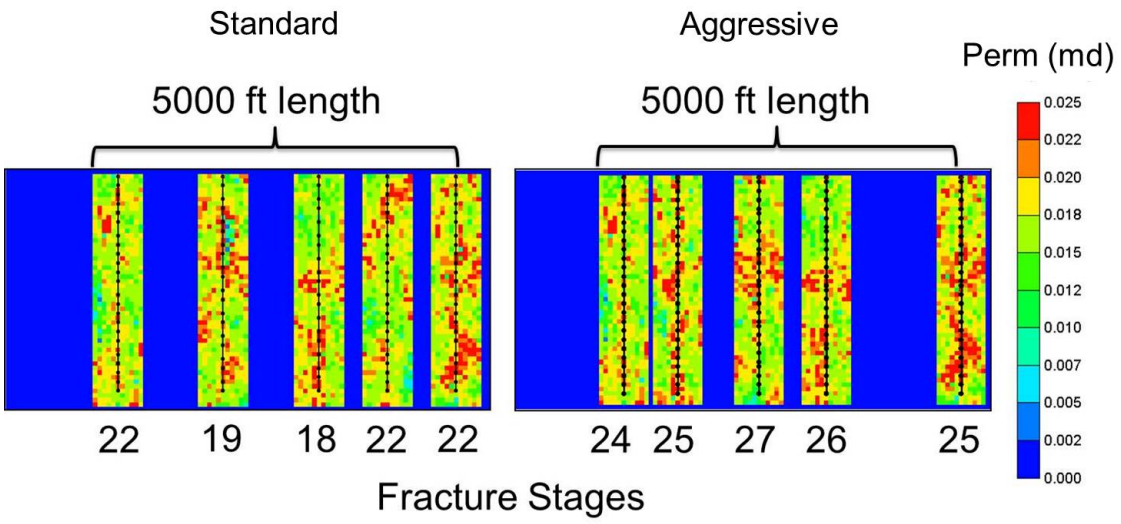

Figure 3.12: Optimized field designs for different economic conditions.

effect of additional production on NPV. With a higher gas price, the marginal benefit is sufficient to justify the use of a greater number of fractures. The well placement also differs between the two cases indicating that some portions of the reservoir may offer better returns depending on the economic conditions.

The two examples presented here demonstrate the flexibility of the surrogate modeling approach. Specifically, the overall procedure was shown to provide fast and accurate optimized field designs for cases with significantly different gas prices and service costs. This framework thus appears to be viable for the optimization of practical shale gas production scenarios.

Chapter 4

Conclusions and Future Work

4.1 Conclusions

In this work, we presented a procedure for optimizing the development of shale gas fields. Starting with a full-physics simulation model, our approach involves the generation of a reduced-physics surrogate model and the subsequent use of this model for the function evaluations (reservoir simulations) required during the optimization. The surrogate model parameters are determined through use of a formal tuning procedure, which essentially "history matches" the surrogate model such that it provides predictions in close agreement with results from the full-physics model. These surrogate models require significantly less computation than the underlying full-physics model, running hundreds of times faster on average. During the course of the optimization procedure, the surrogate model is periodically retrained to ensure continued accuracy.

A generalized pattern search algorithm was applied both to tune the surrogate model and for the field development optimization. In these optimizations, we determined the optimal locations, lengths, and number of fracture stages for a prescribed number of horizontal wells. The effectiveness of the overall procedure was demonstrated for two example problems, where it was shown that the optimization algorithm can account for variations in reservoir quality and direct well placement and fracture intensity to higher quality regions of the reservoir. In the second example, a stronger

economic environment led to optimal well designs with more fracture stages.

Shale gas reservoirs are an important and growing source of natural gas in the United States, and possibly elsewhere, in the future. Because shale resource development is characterized by intensive drilling across thousands of acres, the detailed and time-consuming reservoir simulation workflows developed in recent years may not be appropriate for these reservoirs. Additionally, the wells that are prevalent in shale developments are customizable, with the length of the horizontal section and the number and spacing of hydraulic fracture stages left to the engineer's judgement. With this in mind, new tools such as reduced-physics modeling coupled to optimization may enable a more technical approach for efficiently producing shale resources in the future.

4.2 Directions for Future Work

There are several areas that should be targeted in future work. First, the optimization problem could be expanded to include uncertainty, in either the geology or cost functions. The optimization could then solve for the field design which maximizes expected net present value over an ensemble of geological models. Uncertain future gas prices and capital costs could be incorporated through the use of probability distribution functions. Also, a time component could be included in the placement of the wells. The optimization could consider completing all the wells at once, or drilling a single well to "hold" the lease and then drilling the remaining wells in the future when gas prices may have risen.

Finally, application of the overall procedure to gas condensate and light-oil shale reservoirs should be assessed. The well completions in these fields are similar to those in shale gas formations, so the main modification will be the fluid properties and local geology included in the full-physics model. In gas condensate reservoirs, a reservoir simulator with a compositional, rather than a black-oil, formulation may be required. Compositional simulations are generally computationally expensive, so the use of reduced-physics models, or other surrogate modeling techniques, will be essential.

Nomenclature

C	=	Cost
C_{clay}	=	Clay content
DCF	=	Discounted cash flow
FBHP	=	Flowing bottomhole pressure
G	=	Gas price
GIP	=	Gas in place
GPS	=	Generalized pattern search
GR	=	Gamma ray log value (API units)
i	=	Interest rate
J	=	Tuning procedure objective function
k	=	Permeability
L_i	=	Horizontal section length
mcf	=	Thousand standard cubic feet
MMscfd	=	Million standard cubic feet per day
M_k	=	Permeability multiplier
M_ϕ	=	Porosity Multiplier
n	=	Time step
N	=	Total number of time steps
$N_{f,i}$	=	Number of fracture stages
NPV	=	Net present value
p	=	Pressure
q	=	Period gas production
Q	=	Cumulative gas production

R	=	Royalty rate
SRV	=	Stimulated reservoir volume
S	=	Saturation or number of scenarios
t	=	Time since investment
T	=	Tax rate
$\mathbf{u}$	=	Darcy velocity
V	=	Volume
x_i	=	Well heel location
x_f	=	Fracture half-length

Greek

β	=	Forchheimer correction
γ	=	Specific gravity
μ	=	Viscosity
ν	=	Optimizer iteration
ϕ	=	Porosity
ρ	=	Density

Subscripts

ads	=	Adsorbed
i	=	Initial or well number
L	=	Langmuir property
LOE	=	Lease operating expense
m	=	Matrix property
n	=	Time period
ref	=	Reference solution
s	=	Stimulated zone property
$surr$	=	Surrogate solution
w	=	Water

Appendix A

Idealized Two-dimensional Examples

In this section, we present a variant of the workflow which was applied to an idealized two-dimensional, homogeneous reservoir model. Importantly, the tuning procedure in this section differs from that presented in Section 3.1. Due to the homogenous nature of this reservoir, retraining the surrogate model does not appear to be necessary. In the approach here, the surrogate model is initially tuned to a wide variety of field designs, and then left unchanged during the optimization.

A.1 Idealized Full-Physics Model

The basic properties for the two-dimensional simulation model are summarized in Table A.1. To add some variability and remove symmetry from the reservoir, an initial pressure gradient across the domain is specified (see Fig. A.1); this can be viewed as resulting from depletion in nearby regions. Matrix permeability is 100 nanodarcies, and the fracture conductivities (kw, where k is permeability and w is fracture aperture) are again 2.0 md-ft for primary fractures and 0.4 md-ft for secondary fractures. See Fig. 2.2(b) for a depiction of these two fracture sets. A coarse grid of dimensions $106 \times 53 \times 1$ covering approximately two square miles is used in this example. A $9 \times 9 \times 1$ refinement of this coarse grid is applied in the

Table A.1: Barnett Shale model properties for two-dimensional example

Depth	7000 ft
Porosity	3.0%
$S_{w,i}$	0.3
Initial Pressure	3600 - 4000 psi
FBHP	1000 psi
Grid Dimensions	$106 \times 53 \times 1$
Grid Cell Dimensions	$100 \times 100 \times 300$ ft^3

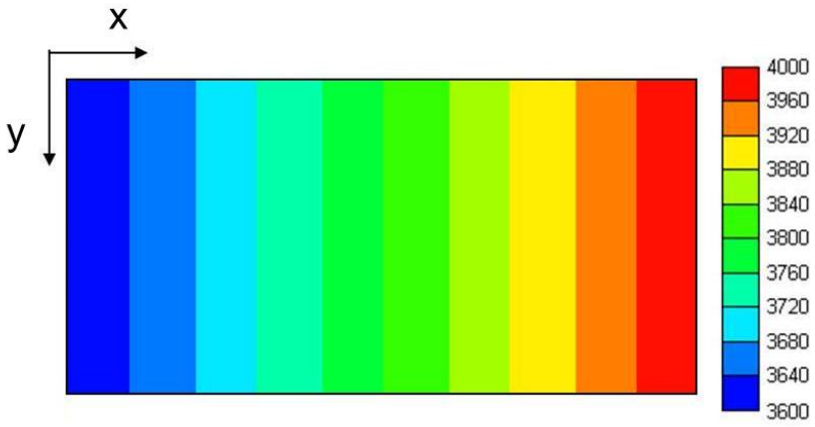

Figure A.1: Areal view of initial reservoir pressure.

stimulated zone, and both primary and secondary fractures are explicitly modeled with refined-grid cells of thickness 2 ft (k is adjusted in these cells such that kw is preserved). The number of grid blocks in the full-physics model depends on the length of the well and the number of fractures, but the typical range is around 50,000 to 250,000 cells.

Table A.2: Development scenarios for surrogate model tuning

Scenario	**Horizontal Length**	**Fractures**
Base case	3000 ft	8 stages
Long well, many fractures	5000 ft	20 stages
Long well, few fractures	5000 ft	4 stages
Short well, many fractures	1500 ft	10 stages
Short well, few fractures	1500 ft	3 stages
Combination	One of each above	

A.2 Reduced-physics Model and Tuning

The reduced-physics models are again tuned with property multipliers as defined in Eq. 2.6. In this case, the matrix properties are homogenous, leading to homogenous stimulated zone properties as well. The reduced-physics model contains 5618 grid blocks, which is a factor of 10 (or more) fewer than a typical full-physics model for this case.

In this example, the surrogate model will be tuned only once, using a variety of scenarios involving multiple wells with different well lengths and well and fracture spacings. The configurations are intended to correspond to field developments that may be encountered during the optimization. Reasonable well and fracture arrangements can be determined prior to the optimization based on knowledge of the constraints (e.g., minimum and maximum fracture spacings) to be used during the optimization.

For validating the tuning procedure, six field development scenarios are considered. The well length and number of fracture stages modeled are shown in Table A.2. For the first five cases, all wells in the model are the same (e.g., all long wells with many fractures, or short wells with few fractures, etc.), while in the last case the wells are all different. These six cases are displayed in Fig. A.2. These configurations are all simulated using the full-physics model. Then, parameters for the surrogate model are computed, as we now describe.

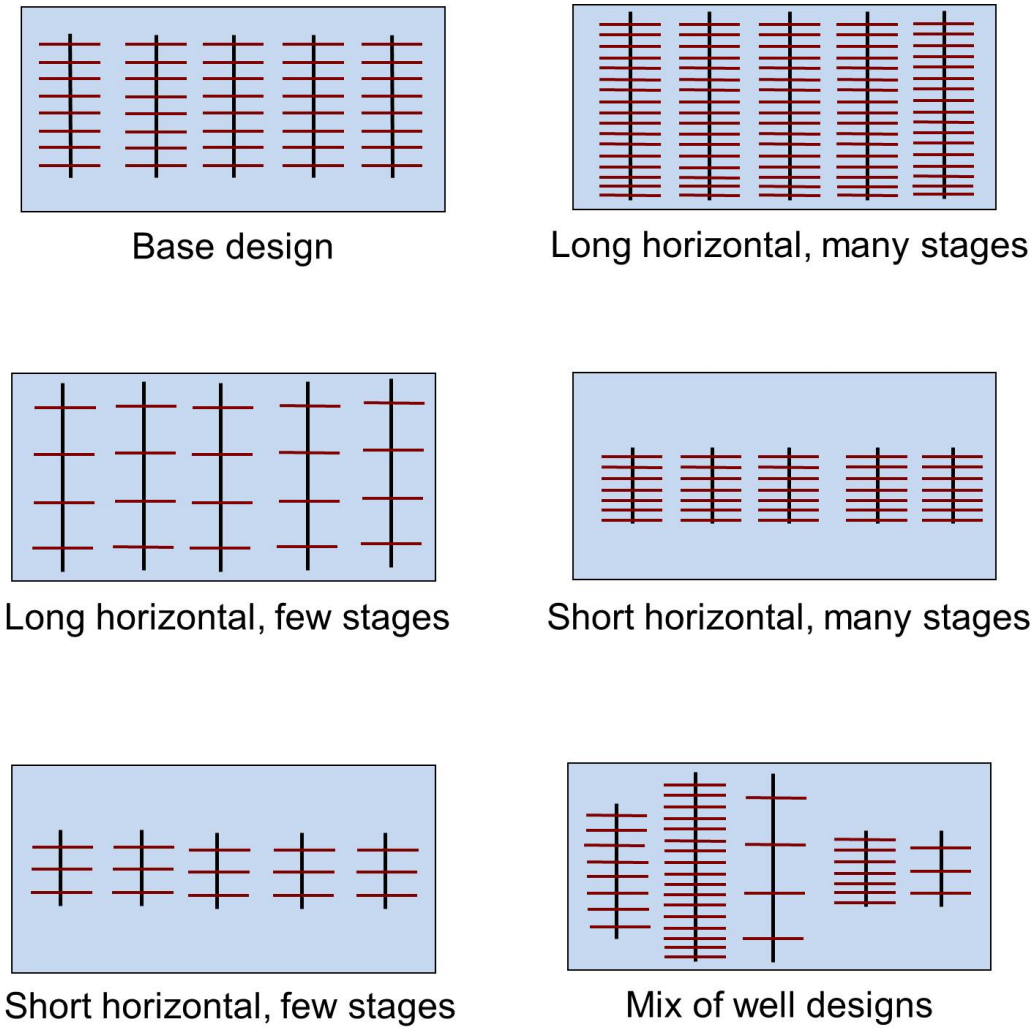

Figure A.2: Well designs used in the tuning procedure.

The quantity we seek to minimize, again denoted by J, is defined as:

$$J = \sum_{s=1}^{S} \sum_{n=1}^{N} \frac{(q_{ref}^{s,n} - q_{surr}^{s,n})^2}{Q_{ref}^{s}\ e^{it_n}}, \tag{A.1}$$

where s indicates the particular scenario and S is the total number of scenarios. Additionally, each scenario is normalized by cumulative production, Q_{ref}^{s}, to give equal weighting to each configuration. An important difference with this technique is that we tune the surrogate model to reduce error over a number of scenarios in Eq. A.1, as opposed to only a single field design in Eq. 2.7. However, the workflow described in Section 2.4 applies retraining, which is not used here.

The minimization problem is again solved using GPS to provide M_ϕ and M_k. The progression of this minimization is shown in Fig. A.3. After nearly 400 function evaluations, the mismatch between the full-physics and surrogate models was reduced by over 95% compared to the initial guess. The initial and optimized SRV properties, along with the optimization constraints, are displayed in Table A.3. The stimulated zone permeability increased by nearly a factor of two, while the increase in porosity was less significant.

Tuning results for two of the six scenarios are shown in Fig. A.4. Importantly, these two scenarios share the same tuned SRV properties, demonstrating the ability of the proxy model to match production results from the full-physics model for a number of field development scenarios. As can be seen by the production responses, the steepness of the decline curve depends on the number of fracture stages and the length of the horizontal wellbore. The tuned surrogate model reproduces the production decline curve of the full-physics model closely in both cases, especially at the crucial early stages of production. For both scenarios shown, the tuned surrogate models run over 100 times faster than the full-physics simulations. This level of speed-up is typical for this two-dimensional case.

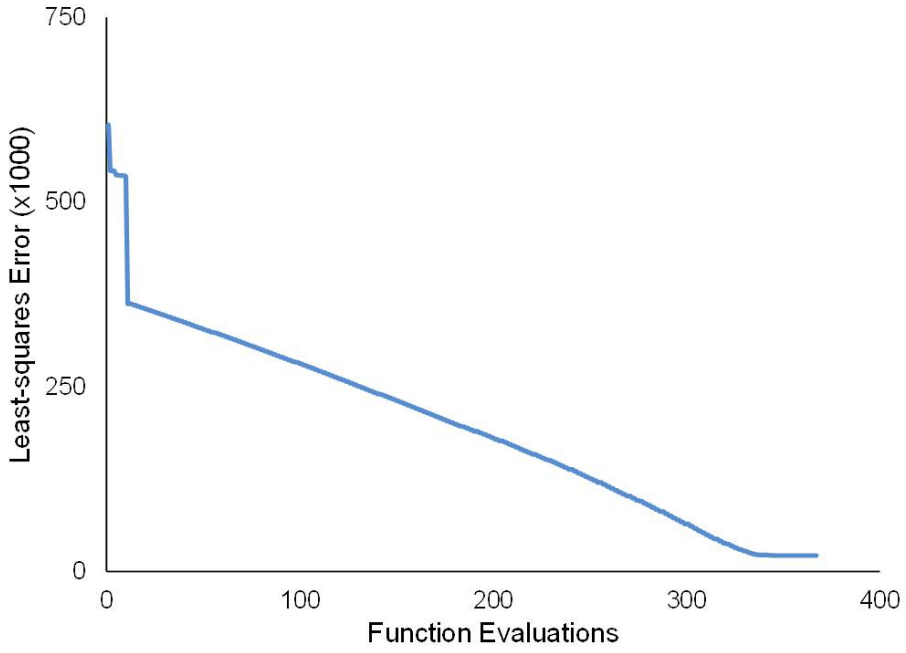

Figure A.3: Optimization performance for tuning the surrogate model.

Table A.3: Initial and tuned SRV properties

Property Multiplier		**Initial**	**Optimized**
M_ϕ	(0.5 - 3)	1	1.27
M_k	(50 - 300)	100	182

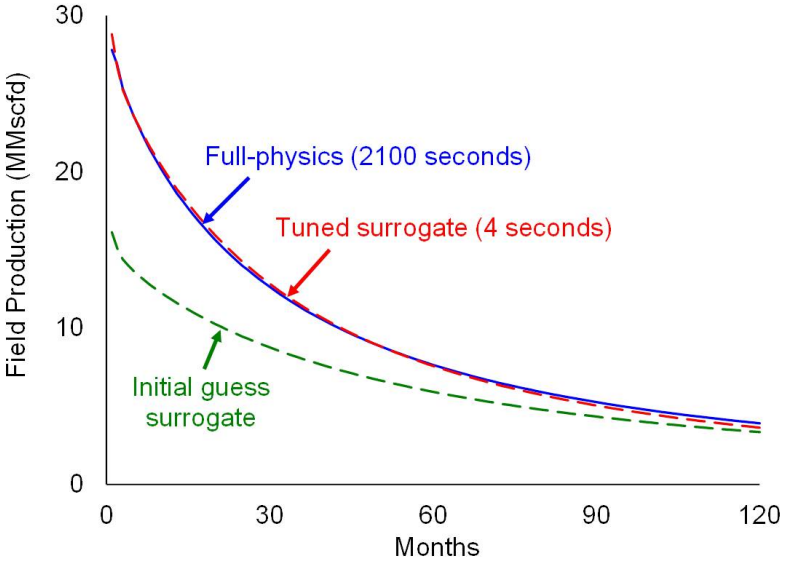

(a) Long wells with many fractures

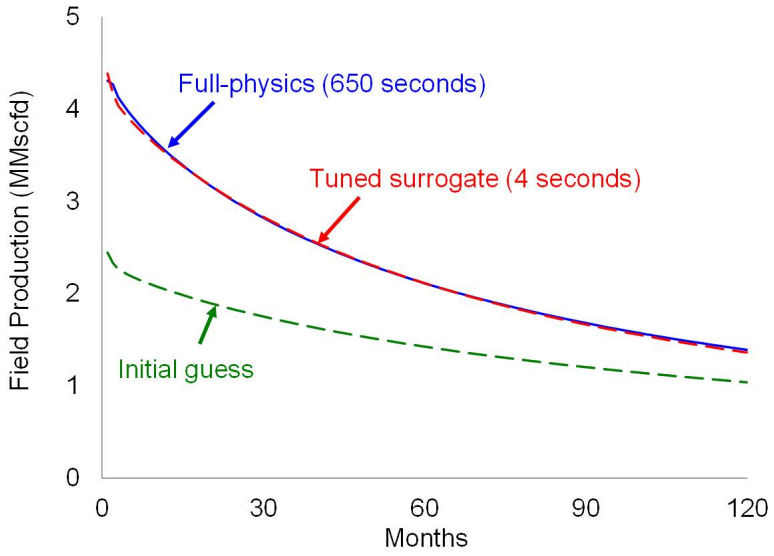

(b) Short wells with few fractures

Figure A.4: Example surrogate tuning results for 2D case.

Table A.4: NPV for initial and converged solutions

	Surrogate	Full-Physics	Error
Initial ($MM)	2.44	2.40	1.7%
Converged ($MM)	14.1	13.9	1.4%
Change	578%	579%	

A.3 Optimization with Gas at $3.50/mcf

We now present results for field development optimization with gas priced at $3.50/mcf. All economic parameters are equal to those displayed in Table 2.3. The initial scenario includes five evenly spaced horizontal wells, 3000 ft in length, with eight fracture stages. The optimization algorithm is expected to shift the well locations toward the portion of the reservoir with higher initial pressure because this region has more gas in place (GIP), which will lead to more production.

The performance of the GPS optimization is shown in Fig. A.5. The blue curve displays results using the surrogate model, while the yellow stars depict results using the full-physics model at the start and end of the optimization. There is clearly very close agreement between the two models for the base case and optimized configurations (see Table A.4 for a detailed comparison), which demonstrates the efficacy of this surrogate modeling procedure for this example. In terms of the actual optimization results, the optimized NPV is nearly a factor of six greater than the base-case NPV. Using the surrogate, each function evaluation requires only a few seconds, so the optimization required less than an hour of computation. The tuning procedure, and full-physics simulation using the optimized development plan, adds another 1-2 hours of computation.

Areal views of the field development plans for the base case and the optimized solution are shown in Fig. A.6. As expected, the optimizer shifts the wells toward the higher GIP region of the reservoir. In addition, the well lengths are the maximum allowed (5000 ft) and the optimized solution uses 16 fracture stages in the two wells located in the highest initial GIP region and 14 stages in the other three wells.

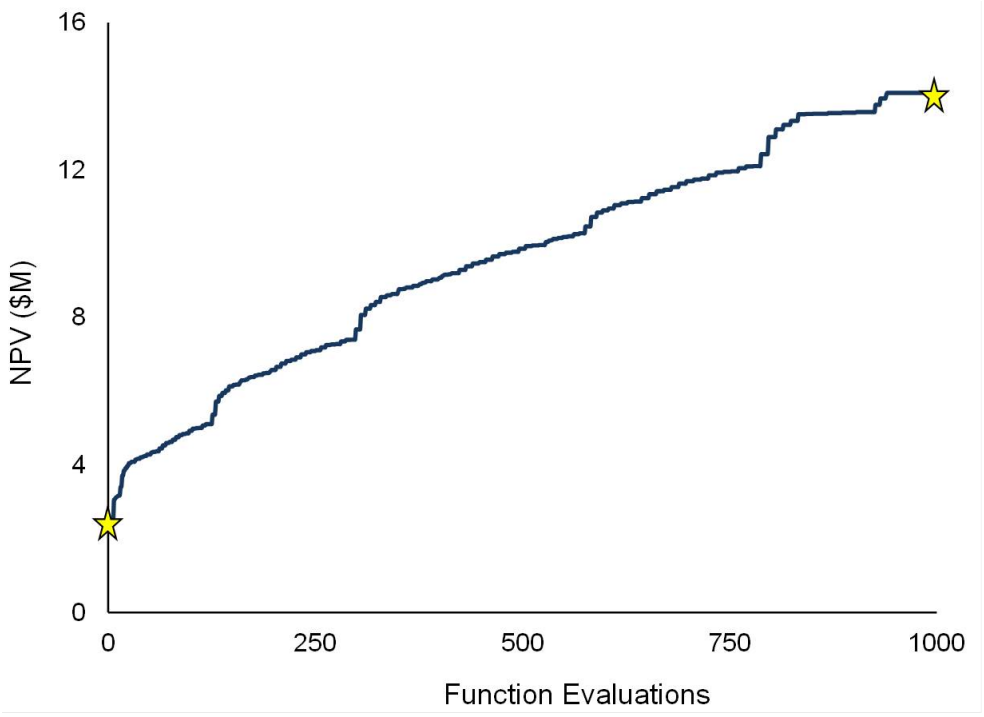

Figure A.5: Field development optimization performance for $3.50/mcf gas.

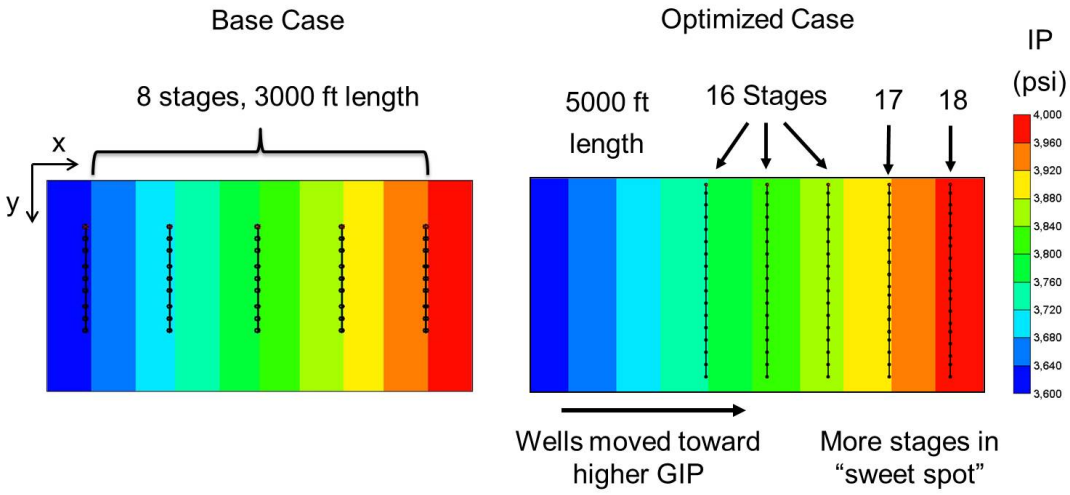

Figure A.6: Areal view of base and optimized field designs. Background shows initial reservoir pressure (psi).

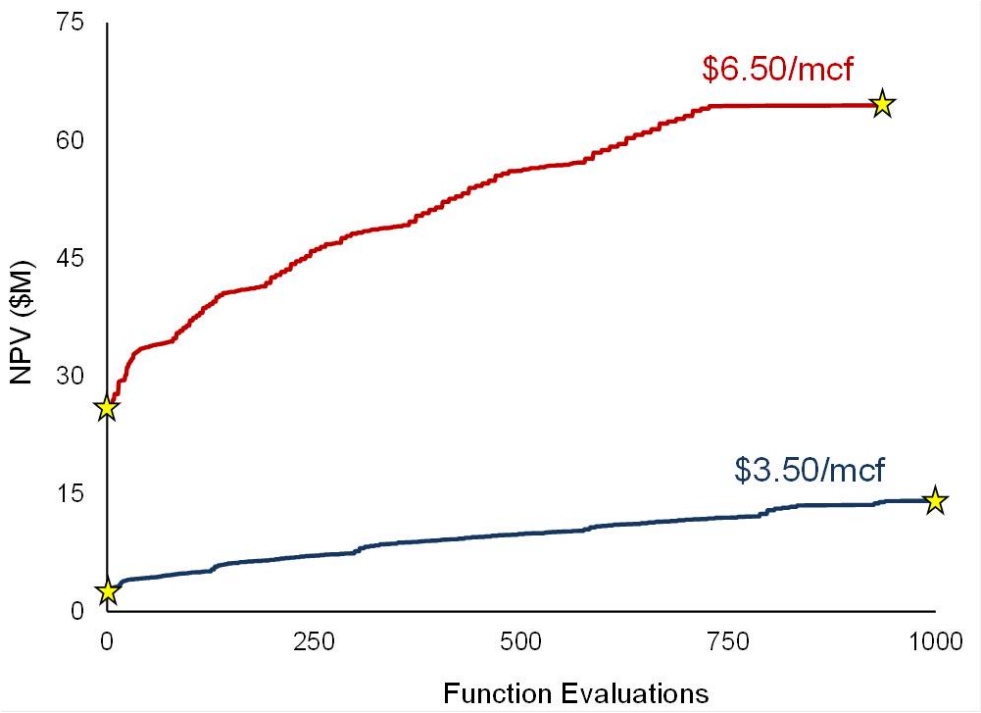

Figure A.7: Optimization performance under different gas price assumptions.

A.4 Optimization with Gas at $6.50/mcf

We now consider a second field development problem, with the gas price increased to $6.50/mcf. All other problem specifications are the same as in the previous example. The idea here is to demonstrate how the optimization algorithm responds to different economic assumptions. The optimization performance and a comparison to the results for the first example are shown in Fig. A.7. Yellow stars again designate full-physics simulations, and close agreement between these results and the surrogate model results is again observed. In this optimization, the base case gives an NPV of $26.0 MM and the optimized solution an NPV of $64.5 MM. It is evident from the figure that the higher gas price results in a much better NPV – a factor of 4.6 greater than that for gas priced at $3.50/mcf. This is because costs such as the expense of the lease and drilling the vertical portion of the well were kept constant between the two examples.

The optimum field development plan is also of interest. As seen in Fig. A.8(a), well

locations and well lengths remain unchanged from the optimum in the first example. However, a greater number of fracture stages are now present in each well. The algorithm thus balances the marginal cost of additional fracture stages ($250,000) with the positive effect of additional production on NPV. Fig. A.8(b) displays the reservoir pressure after ten years of production. Most of the SRV is largely depleted, though a portion of the reservoir remains essentially unchanged. This indicates a possible infill location, or that this reservoir could have supported additional wells. In such a case it may be useful to re-run the optimization using a larger number of wells. Because the overall optimization procedure is quite efficient, a number of different cases can be considered within a reasonable time frame.

We tested the tuning procedure used here on the three-dimensional models with heterogeneous geology described in Section 2.1. We found, however, that this approach did not perform as well as the procedure that used retraining (described in Section 2.4). This may indicate that the use of a single set of (M_ϕ, M_k) leads to some inaccuracy in heterogeneous cases, though it is sufficiently accurate for homogeneous models.

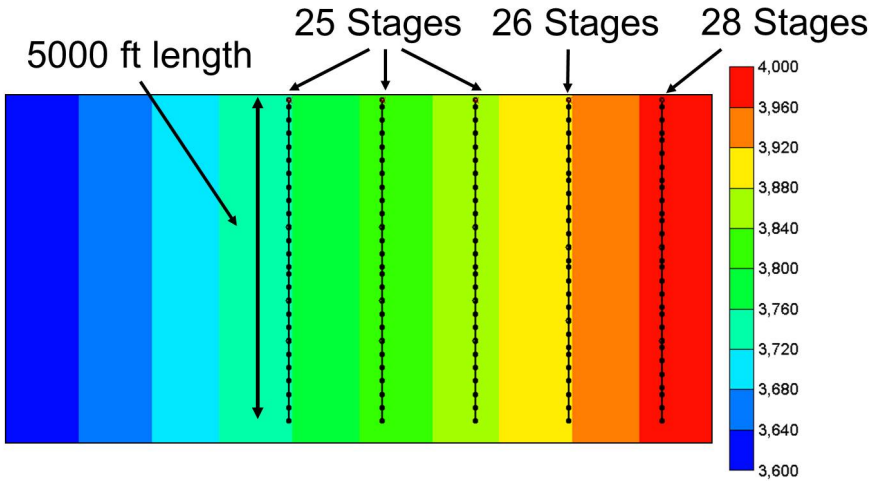

(a) Optimized wells and initial reservoir pressure

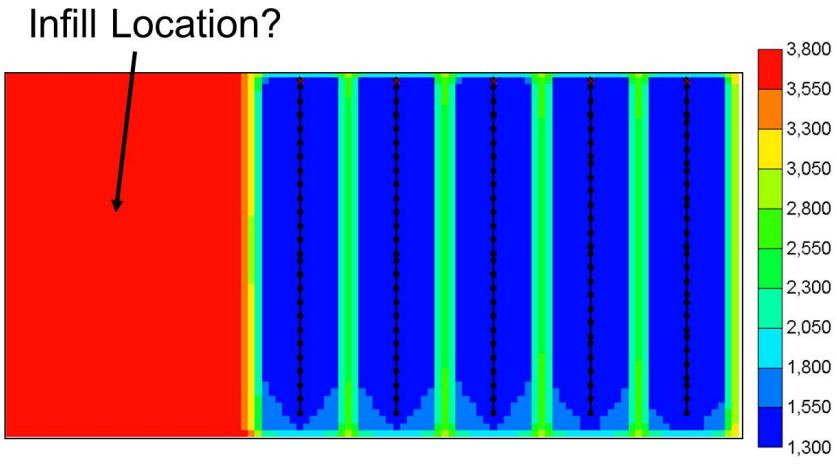

(b) Optimized wells and pressure after ten years of production

Figure A.8: Pressure profiles (in psi) and development scenario for $6.50/mcf gas.

Bibliography

Brouwer D.R. and Jansen J.D. 2004. Dynamic Optimization of Waterflooding with Smart Wells Using Optimal Control Theory. *SPE Journal* **9**(4): 391–402.

Bruner K.R. and Smosna R. 2011. A Comparative Study of the Mississippian Barnett Shale, Fort Worth Basin, and Devonian Marcellus Shale, Appalachian Basin. Technical report, U.S. Department of Energy, Washington D.C.

Cardoso M.A. and Durlofsky L.J. 2010. Use of Reduced-Order Modeling Procedures for Production Optimization. *SPE Journal* **15**(2): 426–435.

Cipolla C.L., Fitzpatrick T., Williams M.J., and Ganguly U.K. 2011. Seismic-to-Simulation for Unconventional Reservoir Development. SPE Reservoir Characterization and Simulation Conference and Exhibition, SPE 146876, Abu Dhabi, UAE.

Cipolla C.L., Lolon E., Erdle J., and Rubin B. 2010. Reservoir Modeling in Shale-Gas Reservoirs. *SPE Reservoir Evaluation & Engineering* **13**(4): 638–653.

Clarkson C.R., Jensen J.L., and Blasingame T.A. 2011. Reservoir Engineering for Unconventional Reservoirs: What Do We Have to Consider? SPE North American Unconventional Gas Conference and Exhibition, SPE 145080, The Woodlands, TX.

CMG 2010. IMEX User's Guide: Advanced Oil/Gas Reservoir Simulator Version 2010. Computer Modeling Group Ltd.

Cowan T. 2011. Costs for Drilling The Eagle Ford. `http://www.rigzone.com/news/article.asp?a_id=108179` Accessed Jan. 10, 2012.

Darling T. 2005. *Well Logging and Formation Evaluation*. Gulf Professional Publishing.

Deutsch C. and Journel A. 1992. *GSLIB - Geostatistical Software Library and User's Guide*. Oxford University Press.

Durst D.G. and Vento M. 2012. Unconventional Shale Play Selective Fracturing Using Multilateral Technology. SPE/EAGE European Unconventional Resources Conference and Exhibition, SPE 151989, Vienna, Austria.

Echeverría Ciaurri D., Isebor O.J., and Durlofsky L.J. 2011. Application of Derivative-Free Methodologies to Generally Constrained Oil Production Optimisation Problems. *Int. J. Mathematical Modelling and Numerical Optimisation* **2**(2): 134–161.

EIA 2012. Annual Energy Outlook 2012 Early Release. Technical report, Energy Information Administration. U.S. Department of Energy, Washington D.C.

Engelder T. 2008. Structural Geology of the Marcellus and other Devonian Gas Shales: Geological Conundrums involving Joints, Layer-Parallel Shortening Strain, and the Contemporary Tectonic Stress Field. AAPG-SEG Eastern Section Meeting Field Trip Guidebook, Pittsburg, PA.

Engelder T., Lash G.G., and Uzcategui R.S. 2009. Joint Sets that Enhance Production from Middle and Upper Devonian Gas Shales of the Appalachian Basin. *AAPG Bulletin* **93**(7): 857–889.

Evans R.D. and Civan F. 1994. Characterization of Non-Darcy Multiphase Flow in Petroleum Bearing Formation. Technical report, U.S. Deparment of Energy Assistant Secretary for Fossil Energy.

Forchheimer P.H. 1901. Wasserbewegung durch Boden [Movement of Water Through Soil]. *Zeitschr Ver deutsch Ing* **49**: 1736–1749.

Forouzanfar F., Li G., and Reynolds A.C. 2010. A Two-Stage Well Placement Optimization Method Based on Adjoint Gradient. SPE Annual Technical Conference and Exhibition, SPE 135304, Florence, Italy.

Frantz J.H., Williamson J.R., Sawyer W.K., Johnston D., Waters G., Moore L.P., MacDonald R.J., Pearcy M., Ganpule S.V., and March K.S. 2005. Evaluating Barnett Shale Production Performance Using an Integrated Approach. SPE Annual Technical Conference and Exhibition, SPE 96917, Dallas, TX.

Gonzalez M.H. and Lee A.L. 1968. Graphical Viscosity Correlation for Hydrocarbons. *AIChE Journal* **14**(2): 242–244.

Jacobi D., Gladkikh M., LeCompte B., Hursan G., Mendez F., Longo J., Ong S., Bratovich M., Patton G., and Shoemaker P. 2008. Petrophysical Evaluation of Shale Gas Reservoirs. CIPC/SPE Gas Technology Symposium, SPE 114925, Calgary, Alberta.

Jarvie D.M., Hill R.J., Ruble T.E., and Pollastro R.M. 2007. Unconventional Shale-Gas Systems: The Mississippian Barnett Shale of North-Central Texas as One Model for Thermogenic Shale-Gas Assessment. *AAPG Bulletin* **91**: 475–499.

Javadpour F. 2009. Nanopores and Apparent Permeability of Gas Flow in Mudrocks (Shales and Siltstone). *Journal of Canadian Petroleum Technology* **48**(8): 16–21.

King G.E. 2010. Thirty Years of Gas Shale Fracturing: What Have We Learned? SPE Annual Technical Conference and Exhibition, SPE 133456, Florence, Italy.

Kolda T.G., Lewis R.M., and Torczon V. 2003. Optimization by Direct Search: New Perspectives on some Classical and Modern Methods. *SIAM Review* **45**(3): 385–482.

Kuuskraa V.A., Schmoker J.W., and Quinn J.C. 1998. Barnett Shale Rising Star in Fort Worth Basin. *Oil and Gas Journal* **96**(21): 67–68, 71–76.

Lu X., Li F., and Watson A.T. 1995. Adsorption Studies of Natural Gas Storage in Devonian Shales. *SPE Formation Evaluation* **10**(2): 109–113.

Marsh E., Sanders P., and Nicks D. 2011. Key Resesource Play Conference Call: Haynesville. Encana Corporate Presentation. `http://encana.com/investors/presentations-events.html` Accessed on Jan. 10, 2012.

Mayerhofer M.J., Lolon E.P., Warpinski N.R., Cipolla C.L., Walser D., and Rightmire C. 2008. What is Stimulated Reservoir Volume (SRV)? SPE Shale Gas Production Conference, SPE 119890, Fort Worth, TX.

Montgomery S.L., Jarvie D.M., Bowker K.A., and Pollastro R.M. 2005. Mississippian Barnett Shale, Fort Worth Basin, North-Central Texas: Gas-Shale Play with Multi-trillion Cubic Foot Potentials. *AAPG Bulletin* **89**(2): 155–175.

Moridis G.J., Blasingame T.A., and Freeman C.M. 2010. Analysis of Mechanisms of Flow in Fractured Tight-Gas and Shale-Gas Reservoirs. SPE Latin American & Carribean Petroleum Engineering Conference, SPE 139250, Lima, Peru.

Onwunalu J.E. and Durlofsky L.J. 2010. Application of Particle Swarm Optimization Algorithm for Determining Optimum Well Location and Type. *Computational Geosciences* **14**: 183–198.

Pollastro R.M., Roberts L.N.R., Cook T.A., and Lewan M.D. 2008. Assessment of Undiscovered Technically Recoverable Oil and Gas Resources of the Bakken Formation, Williston Basin, Montana and North Dakota, 2008. Technical report, U.S. Geological Survey.

Rubin B. 2010. Accurate Simulation of Non-Darcy Flow in Stimulated Fractured Shale Reservoirs. SPE Western Regional Meeting, SPE 132093, Anaheim, CA.

Sarma P. and Chen W.H. 2008. Efficient Well Placement Optimization with Gradient-based Algorithms and Adjoint Models. SPE Intelligent Energy Conference and Exhibition, SPE 112257, Amsterdam, The Netherlands.

Sarma P., Durlofsky L.J., Aziz K., and Chen W.H. 2006. Efficient Real-time Reservoir Management Using Adjoint-based Optimal Control and Model Updating. *Computational Geosciences* **10**: 3–36.

Seidle J.P. and Arri L.E. 1990. Use of Conventional Reservoir Models for Coalbed Methane Simulation. CIM/SPE International Technical Meeting, SPE 21599, Calgary, Alberta.

Standing M.B. and Katz D.L. 1942. Density of Natural Gases. *Transactions of the AIME* **146**(1): 140–149.

Thompson J.W., Fan L., Grant D., Martin R.B., Kanneganti K.T., and Lindsay G.J. 2011. An Overview of Horizontal-Well Completions in the Haynesville Shale. *Journal of Canadian Petroleum Technology* **50**(6): 22–35.

Van Doren J.M.F., Markovinovic R., and Jansen J.D. 2006. Reduced-order Optimal Control of Water Flooding using Proper Orthogonal Decomposition. *Computational Geosciences* **10**(1): 137–158.

Vermylen J.P. and Zoback M.D. 2011. Hydraulic Fracturing, Microseismic Magnitudes, and Stress Evolution in the Barnett Shale. SPE Hydraulic Fracturing Technology Conference and Exhibition, SPE 140507, The Woodlands, TX.

Ward J.A. 2010. Kerogen Density in the Marcellus Shale. SPE Unconventional Gas Conference, SPE 131767, Pittsburgh, PA.

Williams-Kovacs J.D. and Clarkson C.R. 2011. Using Stochastic Simulation to Quantify Risk and Uncertainty in Shale Gas Prospecting and Development. SPE Canadian Unconventional Resources Conference, SPE 148867, Alberta, Canada.

Yang Y. and Alpin A.C. 2010. A Permeability-Porosity Relationship for Mudstones. *Marine and Petroleum Geology* **27**(8): 1692–1697.

Yeten B., Durlofsky L.J., and Aziz K. 2003. Optimization of Nonconventional Well Type, Location and Trajectory. *SPE Journal* **8**(3): 200–210.

Zhao H., Givens N.B., and Curtis B. 2007. Thermal Maturity of the Barnett Shale Determined from Well-Log Analysis. *AAPG Bulletin* **91**(4): 535–549.